



UNIVERSITY OF LEEDS

This is a repository copy of *Determining relative bulk viscosity of kilometre-scale crustal units using field observations and numerical modelling*.

White Rose Research Online URL for this paper:
<http://eprints.whiterose.ac.uk/122473/>

Version: Accepted Version

Article:

Gardner, RL, Piazzolo, S orcid.org/0000-0001-7723-8170 and Daczko, NR (2017)
Determining relative bulk viscosity of kilometre-scale crustal units using field observations and numerical modelling. *Tectonophysics*, 721. pp. 275-291. ISSN 0040-1951

<https://doi.org/10.1016/j.tecto.2017.10.008>

© 2017 Elsevier B.V. This manuscript version is made available under the CC-BY-NC-ND 4.0 license <http://creativecommons.org/licenses/by-nc-nd/4.0/>

Reuse

This article is distributed under the terms of the Creative Commons Attribution-NonCommercial-NoDerivs (CC BY-NC-ND) licence. This licence only allows you to download this work and share it with others as long as you credit the authors, but you can't change the article in any way or use it commercially. More information and the full terms of the licence here: <https://creativecommons.org/licenses/>

Takedown

If you consider content in White Rose Research Online to be in breach of UK law, please notify us by emailing eprints@whiterose.ac.uk including the URL of the record and the reason for the withdrawal request.

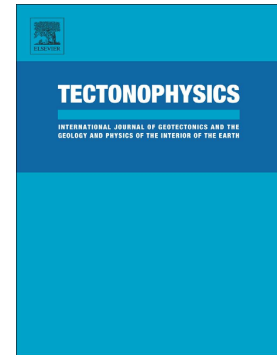


eprints@whiterose.ac.uk
<https://eprints.whiterose.ac.uk/>

Accepted Manuscript

Determining relative bulk viscosity of kilometre-scale crustal units using field observations and numerical modelling

Robyn L. Gardner, Sandra Piazzolo, Nathan R. Daczko



PII: S0040-1951(17)30409-2
DOI: doi:[10.1016/j.tecto.2017.10.008](https://doi.org/10.1016/j.tecto.2017.10.008)
Reference: TECTO 127646
To appear in: *Tectonophysics*
Received date: 19 August 2016
Revised date: 4 October 2017
Accepted date: 6 October 2017

Please cite this article as: Robyn L. Gardner, Sandra Piazzolo, Nathan R. Daczko , Determining relative bulk viscosity of kilometre-scale crustal units using field observations and numerical modelling. The address for the corresponding author was captured as affiliation for all authors. Please check if appropriate. Tecto(2017), doi:[10.1016/j.tecto.2017.10.008](https://doi.org/10.1016/j.tecto.2017.10.008)

This is a PDF file of an unedited manuscript that has been accepted for publication. As a service to our customers we are providing this early version of the manuscript. The manuscript will undergo copyediting, typesetting, and review of the resulting proof before it is published in its final form. Please note that during the production process errors may be discovered which could affect the content, and all legal disclaimers that apply to the journal pertain.

Determining relative bulk viscosity of kilometre-scale crustal units using field observations and numerical modelling

*Robyn L. Gardner¹, Sandra Piazzolo^{1,2}, Nathan R. Daczko¹

¹ARC Centre of Excellence for Core to Crust Fluid Systems and GEMOC, Department of Earth and Planetary Sciences, Macquarie University, NSW 2109, Australia.

²School of Earth and Environment, University of Leeds, Leeds, UK

robyn.gardner@mq.edu.au Phone: 61-2-9850 4728

Abstract

Though the rheology of kilometre-scale polymineralic rock units is crucial for reliable large-scale, geotectonic models, this information is difficult to obtain. In geotectonic models, a layer is defined as an entity at the kilometre scale, even though it is heterogeneous at the millimetre to metre scale. Here, we use the shape characteristics of the boundaries between rock units to derive the relative bulk viscosity of those units at the kilometre scale. We examine the shape of a vertically oriented ultramafic, harzburgitic-lherzolitic unit, which developed a kilometre-scale pinch and swell structure at mid-crustal conditions (~600 °C, ~8.5 kbar), in the Anita Shear Zone, New Zealand. The ultramafic layer is embedded between a typical polymineralic paragneiss to the west, and a feldspar-quartz-hornblende orthogneiss, to the east. Notably, the boundaries on either side of the ultramafic layer give the

ultramafics an asymmetric shape. Microstructural analysis shows that deformation was dominated by dislocation creep ($n=3$). Based on the inferred rheological behaviour from the field, a series of numerical simulations are performed. Relative and absolute values are derived for bulk viscosity of the rock units by comparing boundary tortuosity difference measured on the field example and the numerical series. Our analysis shows that during deformation at mid-crustal conditions, paragneisses can be ~30 times less viscous than an ultramafic unit, whereas orthogneisses have intermediate viscosity, ~3 times greater than the paragneisses. If we assume a strain rate of 10^{-14} s^{-1} the ultramafic, orthogneiss and paragneiss have syn-deformational viscosities of 3×10^{22} , 2.3×10^{21} and $9.4 \times 10^{20} \text{ Pa s}$, respectively. Our study shows pinch and swell structures are useful as a gauge to assess relative bulk viscosity of rock units based on shape characteristics at the kilometre scale and in non-Newtonian flow regimes, even where heterogeneity occurs within the units at the outcrop scale.

Keywords:

Kilometre-scale boudinage; pinch and swell structure; rheology; numerical modelling; polyphase rocks; flow laws.

1 Introduction

The Earth's continental crust is heterogeneous, composed of a large range of rock types of widely varying properties impacting the distribution of stress and strain across the different rock layers during any deformation event (Clark and Royden, 2000). Knowledge of the flow behaviour, or rheological characteristics, of rock units is essential to the quantitative understanding of large scale plate tectonic processes

such as the dynamics of continental break-up, mountain building and topographic evolution (Dahlen, 1984; Beaumont et al., 2001; Groome et al., 2008). Geodynamic numerical models are the main tools used to gain the in-depth understanding required. In these models Earth's dynamic processes are modelled over time spans exceeding, by many orders of magnitude, laboratory and human-life timespans (e.g. Moresi et al., 2003; Moresi et al., 2007; Regenauer-Lieb et al., 2009; Rey et al., 2011). However, for these models to be realistic, it is critical to use accurate large scale flow behaviour for the respective rock units modelled.

Knowledge of the dominant deformation mechanisms and their effect on the flow behaviour at the large scale is at the core of understanding the flow behaviour of rock units (e.g. Dell'Angelo and Tullis, 1989; Shea and Kronenberg, 1993; Stünitz and Fitz Gerald, 1993; Kruse and Stünitz, 1999; Holyoke III and Tullis, 2006b, and references therein). Even though, at any one time a variety of deformation mechanisms act upon a rock simultaneously, their rates differ depending largely on extrinsic parameters such as temperature, pressure, differential stress and grain size (Frost and Ashby, 1972). Therefore, at specific conditions the deformation mechanism with the highest deformation rate will dominate and thus govern the overall flow behaviour of the rock.

A large number of experiments have been undertaken to understand these deformation processes, mostly investigating the behaviour of monomineralic rocks (e.g. quartz: Gleason and Tullis, 1995; olivine: Hirth and Kohlstedt, 2003, Hansen et al., 2011; plagioclase: Rybacki and Dresen, 2004; enstatite: Bruijn and Skemer, 2014, and references therein). For polymineralic rocks there are relatively few laboratory experiments (Shea and Kronenberg, 1993; Holyoke III and Tullis, 2006b; Holyoke III and Tullis, 2006a) with many using rock analogues (e.g. Jordan, 1987;

Dell'Angelo and Tullis, 1996; Herwegh et al., 2003; de Ronde et al., 2005; Dimanov and Dresen, 2005; Farla et al., 2013; Tasaka and Hiraga, 2013; Nishihara et al., 2014; Bystricky et al., 2016; Cyprych et al., 2016). In addition, researchers have used theoretical and numerical approaches (e.g. Reuss, 1929; Voigt, 1928; Handy, 1990; Handy, 1994; Ji, 2004), and rock outcrops (Stünitz and Fitz Gerald, 1993; Fliervoet et al., 1997; Kruse and Stünitz, 1999; Warren and Hirth, 2006; Herwegh et al., 2011; Tasaka et al., 2014; Hansen and Warren, 2015) to derive the rheological laws for polymineralic rocks. However, the deformation behaviours of polymineralic rocks common to the Earths' crust are still under debate (e.g. Bürgmann and Dresen, 2008).

For large geotectonic models it is necessary to model kilometre-scale rock units as a continuum (e.g. Roberts and Houseman, 2001; Moresi et al., 2007; Zhong et al., 2007; Rey and Muller, 2010; Rey et al., 2010; Brune et al., 2014), even though the units are heterogeneous at the millimetre to metre scale. Rocks are commonly polymineralic and rock units are composed of more than a single rock type. Due to this necessity, crustal-scale numerical models commonly simplify the rock unit rheology to values determined from laboratory experiments for quartz, for the upper brittle crust, and either plagioclase or diabase, for the middle to lower crust (e.g. Strehlau and Meissner, 1987; Beaumont et al., 2001; Weinberg et al., 2007; Rosenbaum et al., 2010; Brune et al., 2014). This over simplification can markedly impact the results from the models, consequently there is a need for tools to determine the bulk flow properties of kilometre-scale rock units.

Our knowledge of the rheological properties of specific rock types or layers has been increased by using the geometric characteristics of specific rock structures.

Examples include geological structures at millimetre to metre scale including folds

(e.g. Smith, 1975; Smith, 1977; Ramsay, 1980; Hobbs et al., 2008; Llorens et al., 2013), pressure shadows (e.g. Gresens, 1966; Kenkmann and Dresen, 1998) and high strain zones (e.g. Ramsay and Graham, 1970; Ramsay, 1980; Rennie et al., 2013). Fewer examples exist of investigations where the focus is the rheological interaction between the kilometre-scale rock layers (e.g. Brace and Kohlstedt, 1980; Molnar, 1992; Schmalholz et al., 2002; Tikoff et al., 2002; Frehner et al., 2012; Gueydan and Précigout, 2014).

An important geological structure that can be used to estimate relative viscosities in a multilayered rock package is the pinch and swell structure (e.g. Ramberg, 1955; Smith, 1975; Smith, 1977; Barr and Houseman, 1996; Schmalholz et al., 2008; Schmalholz and Maeder, 2012; Komoróczy et al., 2013; Gardner et al., 2016). These pinch and swell structures form where weak and strong rock layers lie adjacent to one another and are deformed in a pure shear dominated environment (Smith, 1975, 1977; Goldstein, 1988), thereby providing a rough indicator of relative viscosity between the layers. In the central competent layer strain localises to initiate a neck, allowing the less competent matrix to flow viscously into the neck between the swells.

Investigations of the processes of pinch and swell initiation and formation have commonly used micro-scale and outcrop-scale structures (e.g. Lohest et al., 1908; Cloos, 1947; van der Molen, 1985; Schmalholz et al., 2008; Schmalholz and Maeder, 2012; Gardner et al., 2016), though lithospheric-scale necking to form rifted basins has also been reported (e.g. Zuber and Parmentier, 1986). Analogue experiments have concentrated mainly on pinch and swell structures in non-Newtonian flow regimes (Neurath and Smith, 1982; Kobberger and Zulauf, 1995; Zulauf and Zulauf, 2005; Mengong and Zulauf, 2006). The refinement of numerical models has allowed

more detailed analysis of the impact of the viscosity ratio between adjacent layers in both Newtonian and non-Newtonian flow regimes (Abe and Urai, 2012; Schmalholz and Maeder, 2012; Komoróczy et al., 2013; Gardner et al., 2015; Gardner et al., 2016).

In all cases, the structures used consist of one rock type forming the middle competent layer, and another rock type on either side of the central layer. This type of scenario is typically seen at the outcrop scale where, for example, an intruding dyke is deformed post-intrusion together with its host rock. However, at the kilometre scale it is common to observe individual rock packages characterized by multiple rock units of variable competency throughout; hence the pinch and swell structure can develop within a three-layered structure, with the competent layer surrounded by rock units of contrasting competency on either side.

Recently, Gardner et al. (2016) utilised a three-layered structure to develop a modified viscosity ratio gauge, using the shape asymmetry of the pinch and swell structures to determine the bulk viscosity ratio between the rock units by measuring the tortuosity of the boundaries on either side of the central competent unit. The absolute difference between the two tortuosity measurements (tortuosity difference, T_D) provides a measure for the asymmetry of the pinch and swell shape where a value of $T_D > 0.05$ signifies a detectable asymmetric shape with contrasting viscosity either side of the competent layer. By comparison with a series of numerical models, the bulk viscosity ratio of the surrounding layers can be determined to the first order. In their study, Gardner and co-workers focused on a centimetre-scale structure within lower crustal rocks showing that the simplified use of an experimentally determined plagioclase flow law may underestimate the viscosity of typical polymineralic, lower crustal rocks by up to 40 times. Based on microstructural

analysis of a representative field example, the general flow law inferred and used in those numerical models was Newtonian viscous. In principle, the technique of Gardner et al. (2016) should also work for materials deforming in the non-Newtonian flow regime. Importantly, the method used by Gardner et al. (2016) can be applied, not only on the centimetre to decimetre scale, but also the kilometre scale, allowing assessment of relative bulk viscosity ratios of whole rock units, even where internal heterogeneities exist at the centimetre to metre scale.

To our knowledge, even though some examples of kilometre-scale pinch and swell structures have been described in general terms in the geological literature, so far they have not been investigated in detail. For example, kilometre-scale pinch and swell structures where the competent layer consists of ultramafic rocks have been mapped in the Honeysuckle Complex and Coolac Serpentinite in New South Wales (Stuart-Smith, 1990), the Isua Terrane (Nutman and Friend, 2009) and Ussuit area (van Gool and Marker, 2007) in south-western Greenland, and the Western Gneiss Region in the Scandinavian Caledonides (van Roermund, 2009).

In this contribution, we apply the new viscosity gauge tool presented by Gardner et al. (2016), to an asymmetric kilometre-scale pinch and swell structure, which developed during middle crustal deformation, in the Anita Shear Zone (ASZ) in Fiordland, New Zealand (Hill, 1995; Klepeis et al., 1999; Fig. 1a). Our study aims to derive the bulk viscosity of the rock units, where the bulk viscosity is the viscosity of the unit at the kilometre scale. In the field area, a vertically-oriented ultramafic unit forms the competent layer and is surrounded by paragneiss and orthogneiss on either side of the ultramafic layer. We first present field data to determine the tortuosity difference, along with detailed microstructural analysis, to determine the dominant deformation mechanism for the ASZ rock units. Further, we perform

numerical simulations that are then compared to the tortuosity difference field data to determine the bulk viscosity ratio between the ultramafic layer and its surrounding gneisses.. Our results show that during deformation the orthogneiss and paragneiss can be approximately 13 and 32 times less viscous, respectively than the ultramafic unit. Bulk viscosity of the ultramafic unit is estimated and the effective viscosity ratios from the numerical model then allow the calculation of the bulk viscosity of the kilometre-scale gneissic units. In addition, results show that the highest stresses across the pinch and swell structure during deformation occur at the layer-matrix boundary between layers of different rheology, in both the competent and weaker surrounding layers.

Using the shape characteristics of the pinch and swell structure allows, for the first time, the viscosity contrast between rock units to be determined from field observations of a heterogeneous crustal package at the kilometre scale. This method could prove useful for constraining the viscosity parameters necessary for large-scale numerical modelling currently used to understand controversial issues such as crustal channel flow, hyperextension, and lower crustal flow, with the associated mountain building processes.

2 Field results and interpretation

2.1 Geological background

The Anita Shear Zone (ASZ) lies in the Fiordland World Heritage Area, near Milford Sound, New Zealand (Fig. 1a inset) and represents a ~4 kilometre-wide, mid-crustal amphibolite facies shear zone (Fig. 1a). It comprises four geological units (Wood, 1972): (i) St Anne Gneiss and (ii) Thurso Gneiss of the Paleozoic Tuhua Sequence, (iii) Anita Ultramafics of unknown age forming a pinch and swell structure, and (iv)

Jagged Gneiss, part of the Arthur River Complex that includes a mix of Paleozoic (Ireland and Gibson, 1998; Tulloch et al., 2011) and Mesozoic orthogneisses (Hollis et al., 2003). The Anita Ultramafics form a pinch and swell structure at the kilometre scale.

Structural analysis of the ASZ (Klepeis et al., 1999) defined four deformation phases, with the initial phase being recognized by a sub-horizontal to gently east or west dipping layering. This initial foliation is deformed into tight to isoclinal, recumbent to inclined, gently NE-plunging folds in the second phase. The subsequent D_3 phase (Klepeis et al., 1999) is the main shear zone forming phase, and is characterized by sub-vertical foliation and sub-horizontal lineation indicating NE-SW directed stretching, with a kinematic vorticity of 0.54. This vorticity means the D_3 deformation phase has both a rotational (simple shear) and non-rotation (pure shear) component. However, a vorticity value between 0 and 0.75 indicates that the pure shear component dominates (Tikoff and Fossen, 1995). The D_3 structural fabric is dominant across the ASZ, and in general, is near parallel to the ASZ and lithological boundaries. The subvertical D_3 foliation intensifies in localized high strain zones (HSZ) at the contacts of the Anita Ultramafics with the surrounding gneisses. Hence, the formation of the pinch and swell structure and the HSZs are interpreted to be part of the D_3 event. The temperature of the D_3 event is ~ 600 °C and ~ 8.7 kbar (Klepeis et al., 1999; Clarke et al., 2000; Czertowicz et al., 2016c). The fourth deformation phase is characterized by cataclastic textures and crenulation cleavage cross-cutting the previous deformation phases (Klepeis et al., 1999). Exhumation occurred in the Cretaceous, c. 104 Ma (Czertowicz et al., 2016a) during the extension and breakup of the Pacific margin of Gondwana (Klepeis et al., 1999). In this contribution, we

examine in detail the structures associated with the main shear zone forming D_3 event.

2.2 Methods

The Anita Ultramafics form a pinch and swell structure at the kilometre scale. Samples and structural data were collected from around Lake Ronald (Fig. 1 and 2). The ultramafic swells form prominent, steep outcrops, approximately one kilometre wide to the north and south of the lake, with sparse, hardy foliage allowing good access to outcrops and samples. By contrast, the gneisses are recessive units covered with dense forest and impenetrable undergrowth, rendering access to well exposed outcrops for in-situ sample acquisition, more difficult.

The intensity of foliation, is defined by the layer continuity and spacing at the outcrop scale, and is used as a first approximation of strain intensity (e.g. Watts and Williams, 1983). In the field, high strain is interpreted where foliation has sub millimeter-scale spacing of continuous, differently coloured bands (Fig. 3).

We measure the tortuosity of the boundaries on either side of the central ultramafic unit. The tortuosity of a boundary is the ratio of the length of the layer boundary and a straight line (for details, see Gardner et al. (2016)). The absolute difference between the tortuosity measurements on either side (tortuosity difference, T_D), provides a measure of the symmetry of the pinch and swell shape, where, as defined by Gardner et al. (2015) $T_D < 0.05$ and $T_D > 0.05$ signify symmetric and significant asymmetric shape, respectively.

Samples of representative rock types, displaying variable amounts of strain, were collected along a cross section of an Anita Ultramafics swell (Fig. 1a, red arrow) and the surrounding gneisses (Fig. 3). Variably strained samples of each rock type (Fig.

1 and 2) were cut parallel to stretching lineation (X) and perpendicular to foliation (XY). For initial analysis of the microstructures, polished thin sections were examined using a petrographic microscope, in conjunction with the virtual petrographic microscope (Tetley and Daczko, 2014). To assess the degree of recrystallisation experienced by the ultramafic samples we have determined the area percentage of relict grains, that is, those grains with an area larger than $100 \times 100 \mu\text{m}^2$ ($> 0.01 \text{ mm}^2$), using ImageJ (Rasband, 2013) to analyse a high resolution image of the whole thin section. Subsequently, quantitative microstructural analysis was performed using Electron Backscatter Diffraction (EBSD) analysis on microstructures typical for each rock type and strain variation. For the latter, thin sections were polished using colloidal silica and coated with $\sim 3 \text{ nm}$ of carbon. Crystallographic orientation information was collected using an HKL NordlysNano detector attached to a Zeiss IVO scanning electron microscope (SEM) at the Geochemical Analysis Unit, Macquarie University. The SEM was run at a high vacuum with an accelerating voltage of 20 kV, a working distance of 12 mm and a beam current of 8.0 nA. Points were analysed on a regular grid with step sizes between 2 and 6 μm for the ultramafic samples and 3 and 10 μm for the gneissic samples, depending on the grain size and spatial detail needed. The Kikuchi patterns acquired were automatically indexed using the Aztec analysis software (Oxford Instruments). Concurrently, chemical maps were taken using an X-Max energy dispersive spectrometry (EDS) detector allowing an independent control on mineral type and abundance.

Data was processed using HKL Channel5 v5.11, with noise reduction performed on the raw data following the procedure of Bestmann and Prior (2003), Piazzolo et al. (2006), and Prior et al. (2002). Phase maps of a representative subset of the

complete map acquired are shown (cf. Fig. 6 and 7), along with equal area, lower hemisphere pole figures of the main minerals, constructed using data from the complete map based on one point per grain in grey scale. Representations using one point per grain eliminate the issue of large grains distorting the interpretation by causing single crystal maxima in the pole figures. For comparison, the relative crystal orientation change of the large, relict grains is provided as a graded colour scale overlay on the phase maps and pole figures. Misorientation angles between adjacent analysed points $\geq 10^\circ$ define grain boundaries, whereas misorientation angles of 2 - 10° define sub-grain boundaries. Misorientation angle distributions (MAD) are presented as histograms for adjacent (or correlated) pairs and random (or uncorrelated) point pairs (cf. Fig. 6 and 7, blue and red histogram columns, respectively). For reference, the theoretical random distribution is also depicted (cf. Fig. 6 and 7, black lines on the histograms). To determine quantitatively the strength of the preferred crystal orientation, the M-index (Skemer et al., 2005) for the main minerals in each sample was calculated using the numerical application MTEX (Mainprice et al., 2015) on the EBSD derived average crystallographic orientation for each grain. Shape preferred orientation (SPO) was plotted as a rose diagram from the EBSD orientation grain data for each sample, where an angle of 90° is parallel to lineation.

2.3 Results

2.3.1 Field observations

The Anita Ultramafics unit forms a pinch and swell structure at the kilometre scale characterized by variations in unit thickness along strike with thin and thick necks developed (Fig. 1a, blue and yellow arrows) between swells. Thin necks form where

strain is highly focussed into narrow zones, whereas thick necks form where strain localisation is less focussed (Gardner et al., 2015). Detailed geological mapping to the north and south of Lake Ronald (Fig. 2a) confirmed the previously reported (Klepeis et al., 1999; Turnbull et al., 2010; Czertowicz et al., 2016a) general sub-vertical S_3 foliation, with a sub-horizontal to gently NE or SW plunging lineation (Fig. 2a, c and d).

For the authors to measure tortuosity, the position of the lithological boundaries needed to be determined. Although the terrain is extremely rugged, and areas of moraine occur, the boundaries of the Anita Ultramafics could be determined with high accuracy (Fig. 1a, Fig. 2a and b). This is due to the fact that (i) the sparse vegetation on the ultramafic unit changes dramatically at the contact with the gneisses and (ii) the boundaries are close to vertical (Fig. 1a, 2a, b and c). The position of the boundaries in inaccessible areas is based on the extrapolation of foliation curvature (here S_{MyI}) in the adjacent rock units as mapped in the field by the authors and data from Czertowicz et al. (2016a) and Klepeis et al. (1999). This extrapolation may cause some inaccuracy in the calculated tortuosity. Estimates of tortuosity accuracy provided are based on results obtained from extrapolations by multiple geologists interpreting the mapped and measured structural data. For example, in the case of Lake Ronald in the ASZ, extrapolation of the western boundary under the lake varies the tortuosity difference measurement in the order of 0.005.

The Anita Ultramafics to Jagged Gneiss boundary, at the kilometre scale, is relatively straight, compared with the boundary to the Thurso Gneiss (Fig. 1a, 2a and b), giving the ultramafics an asymmetric shape (Fig. 1a, 2a and b) parallel to the NE-SW extension direction. Based on our field data, in combination with previously published

data the tortuosity of these boundaries was measured at two scales (Fig. 1a, B₁, and Fig. 2b, B₂), providing a significant tortuosity difference of $\sim 0.09 \pm 0.01$ and $\sim 0.10 \pm 0.03$ for T_{D1} and T_{D2}, respectively.

The centre of the Anita Ultramafics is characterized by centimetre to tens of metre thick bands of differing compositions (Fig. 4). Pure harzburgite is the dominant rock type, with bands of harzburgite with > 15% talc, from 10 cm to ~40 m wide (Fig. 4a). In addition, infrequent narrow bands, up to 10 cm wide, of clinopyroxene dominated lherzolite (Fig. 4b), and up to millimeter width chromite bands are found within the harzburgite. In the centre of the ultramafics the boundaries of these compositional bands (e.g. strike and dip measurements of 162/38/NE) are at an angle to the strike of the general S₃ foliation (e.g. 194/78/W) with significant steepening of foliation close to lithological boundaries. (Fig. 2a; yellow and red symbols, respectively). The compositional bands are macroscopically dragged into the D₃ tectonic foliation closer to the ultramafic boundary with the Thurso Gneiss (e.g. 007/88/E).

On the Ultramafics to Jagged Gneiss boundary there is a very narrow (~15 m) HSZ in the ultramafic unit with a wider (~160 m) HSZ in the orthogneiss (Fig. 2b). The HSZs are defined as zones with consistent steep foliation, sub-millimetre-scale spacing of foliation and significant grain size reduction. A wider, much more variable HSZ is seen on the Anita Ultramafics to Thurso Gneiss boundary, with a HSZ of ~200 m within the ultramafic unit and a width larger than 500m within the Thurso Gneiss (Fig. 2b).

Samples of the Anita Ultramafics taken in the HSZ near the Thurso Gneiss are typically fine grained layered harzburgite, with minor olivine porphyroclasts displaying elongated, recrystallised tails and a strong foliation (Fig. 3b). The samples in the centre of the ultramafics are coarser grained with higher proportions of

porphyroclasts and less obvious foliation than their high strain equivalents (Fig. 3c).

The sample from the HSZ near the Jagged Gneiss is again, a finely layered harzburgite with minor olivine porphyroclasts (Fig. 3d).

The Thurso Gneiss is a heterogeneous meta-sedimentary quartz-hornblende-plagioclase-biotite felsic package with minor calc-silicate to marble (Wood, 1972; Hill, 1995). The sample taken adjacent to the Anita Ultramafics is fine grained gneiss with thin mafic and felsic laminations (Fig. 3a). The Jagged Gneiss is a mafic plagioclase-hornblende-quartz-garnet gneiss (Wood, 1972; Hill, 1995). The sample taken near the Anita Ultramafics is a mylonitic amphibole and garnet bearing gneiss with felsic porphyroclasts displaying elongated, recrystallised tails (Fig. 3e).

2.3.2 Petrography and Microstructures

In the following sections and in Figures 5 and 7 we provide microstructural data of the gneissic and ultramafic samples, while summaries are given in Table 1 and Figure 8.

2.3.2.1 *Thurso paragneiss*

In the map area all outcrops of Thurso paragneiss (e.g. Fig.3a; AS1304) show high strain, fine grained mylonites of predominantly plagioclase (~41 area %, grain size 42.6 μm), quartz (~31 area %, grain size 34.3 μm) and biotite (~22 area %, grain size 75 μm), with minor garnet, amphibole, epidote and opaques (together, ~5 area %) occurring in thin layers. The foliation is defined by continuous bands of biotite wrapping around larger quartz and plagioclase grains (Fig. 5a). Aspect ratios for plagioclase and quartz are similar at $\sim 1.6 \pm 0.5$ with biotite displaying high aspect ratios of ~ 7.0 (Fig. 5a). Quartz grains show undulose extinction and presence of subgrains. Plagioclase additionally displays some deformation twinning. Plagioclase shows a weak crystallographic preferred orientation (CPO) (Fig. 6a, pole figures; M-

index = 0.01). Quartz has a moderate CPO (Fig. 6a, pole figures; M-index = 0.04), with the {0001} forming a girdle $\sim 30^\circ$ from the XZ plane and a non-random MAD skewed to lower angle boundaries. The optically determined preferred orientation of biotite is confirmed by a very strong CPO (Fig. 6a, pole figures; M-index = 0.10) with {100} generally parallel to lineation and the {001} perpendicular to foliation, and a strongly non-random MAD.

2.3.2.2 Anita Ultramafics: Centre

The sample from the centre of the Anita Ultramafics (Fig. 3c; AS1309) has 85 area % olivine, with 15 area % opaques and talc (Fig. 5c). Large, elongate, relict olivine grains with sizes $> 0.01 \text{ mm}^2$ occupy $\sim 10\%$ by area, define the foliation and display irregular grain boundaries (Fig. 5c). Undulose extinction and subgrains are seen in the olivine porphyroclasts showing progressive rotation of the crystal orientation across the grain (Fig. 5c and 7c, EBSD phase map with relative orientation change for the large grain in shades of aqua). They are up to 5 mm in size and are surrounded by an olivine matrix of variable smaller, recrystallised grain sizes (44.9 μm ; Fig. 5c). Aspect ratios for olivine are variable (1.7 to 2.2), with the larger grain sizes having higher aspect ratios. SPO has a maximum close to lineation and all grains are within 45° of the lineation (Fig. 7c histogram). Small grains have rare 120° junctions, show some lobate boundaries and are larger in the strain shadows of porphyroclasts (Fig. 5c). Fine grained olivine has a relatively weak CPO (Fig. 7c pole figures; M-index = 0.02) and near random MAD and is similar to that of olivine porphyroclasts (Fig. 7c, olivine pole figure).

2.3.2.3 Anita Ultramafics: near Thurso Gneiss

Ultramafic samples near the Thurso unit boundary include a fine grained harzburgite (AS1305A2) with less than 1% of relict grains, taken at a distance of $\sim 50 \text{ m}$ from the

ultramafic to paragneiss boundary. It is characterized by olivine (85 area %), enstatite (11 area %) and opaques (4 area %). A second, slightly lower strain sample (AS1306B) consisting also of a fine grained harzburgite was taken an additional ~75 m further from the boundary. It has a high area percent of olivine (81 area %), of which ~1 area % are relict grains, 15 area % enstatite and 4 area % opaques.

Olivine grain sizes in the matrix are very fine (20.0 μm) in the sample closest to the ultramafic boundary, and slightly larger (23.9 μm) further from the boundary (Fig. 8b).

In both samples, the foliation is defined by fine bands of opaques, and only the rare larger olivine grains show undulose extinction and subgrains showing progressive rotation of the crystal orientation across the grain (Fig. 7b). Olivine grains have aspect ratios of 1.8 ± 0.5 and 1.7 ± 0.3 , respectively. All olivine grains have some lobate to irregular boundaries and slightly larger grain sizes in the strain shadows of porphyroclasts where there is no enstatite (Fig. 5b). In the sample nearest to the Thurso Gneiss (Fig. 7a), enstatite is dispersed throughout the olivine with very fine grain sizes (12.9 μm). Further from the Thurso Gneiss boundary, the enstatite has larger grain sizes (15.4 μm ; Fig. 8b) and forms bands parallel to the foliation.

Olivine has the same M-index and similar CPO for both samples (Fig. 7a and b, pole figures; Fig. 8a; M-index = 0.07), where {100} and {001} are parallel to foliation and {010} is perpendicular to foliation. By contrast, enstatite in the sample closest to the boundary (AS1305A2; Fig. 7a) has stronger CPO (M-index = 0.05) compared to the sample further from the boundary (Fig. 7b, pole figures; Fig. 8a; M-index = 0.01).

Both olivine and enstatite have SPO close to the lineation for the sample closest to the boundary, but SPO is random for enstatite in the sample further from the boundary.

2.3.2.4 Anita Ultramafics: near Jagged Gneiss

The highly strained harzburgite sample (Fig. 3d; AS1330) from the narrow ultramafic HSZ comes from within ~5m of the boundary with the orthogneiss (i.e. Jagged Gneiss). It consists of olivine (80 area %), enstatite (13 area %) and opaques and talc (7 area %) with ~1% of relict olivine grains (Fig.8c). Aspect ratios for olivine (2.2 ± 1.0) and enstatite (1.6 ± 0.5) are variable, with the larger grain sizes having higher aspect ratios; together with the alignment of fine grained enstatite (16.8 μm) they define the foliation. Undulose extinction is seen only in the larger olivine grains where crystallographic orientation can vary up to $\sim 10^\circ$ (Fig. 7d). Different to the irregular boundaries of porphyroclasts, small olivine grains (28.2 μm) rarely show lobate boundaries with slightly larger grains in the strain shadows of porphyroclasts where there is no enstatite (Fig. 5d).

Olivine has a high M-index = 0.13 (Fig. 8a) with {100} and {001} parallel to foliation and {010} planes perpendicular to foliation. CPO for the large olivine porphyroclasts is similar to that of the smaller olivine grains (Fig. 7d, olivine pole figures). Enstatite in this sample has a very weak CPO (Fig. 7d, pole figures; Fig. 8a; M-index = 0.003).

2.3.2.5 Jagged Gneiss

Two samples of the Jagged Gneiss are examined; a low strain sample from more than 200 m from the ultramafic to orthogneiss boundary (Fig. 5f) and one originating from the HSZ within 50 m to the boundary with the ultramafic (Fig. 5e). The orthogneiss is relatively homogenous, composed of predominantly quartz (~39 area %), plagioclase (~35 area %) and amphibole (~10 area %) with minor garnet, biotite and opaques (together, 16 area %). Grain sizes for quartz (up to 0.7 mm), plagioclase (up to 1 mm) and hornblende (up to 0.3 mm) in the low strain sample (Fig. 5f; AS1315F) are coarser than in the higher strain sample (Fig. 3e and 5e;

AS1316), 15.2 μm , 17.5 μm and 13.4 μm , respectively. The mineral SPO, particularly in hornblende, and contrasting light (quartz and plagioclase) and dark bands (amphibole and opaques) define the foliation. Aspect ratios for quartz and plagioclase are 1.8 ± 0.6 and 1.7 ± 0.6 , respectively, while those of hornblende are higher (2.2 ± 1.1). Quartz grains in the lowest strained sample (e.g. Fig. 5f) display undulose extinction and subgrains, while, additionally, plagioclase grains display minor deformation twinning. The high strain sample shows fewer subgrains and less undulose extinction for both plagioclase and quartz, with additionally, minor deformation twinning for plagioclase (Fig. 5e).

In the high strain Jagged Gneiss sample plagioclase has a very weak CPO (Fig. 6b pole figures; M-index = 0.02) for all grain sizes. Quartz exhibits a weak to moderate CPO (Fig. 6b pole figures; M-index = 0.05), with $\{0001\}$ forming a weak distributed girdle on the YZ plane. Hornblende shows internal deformation features such as distinct subgrain boundaries (Fig. 6b) and forms a very strong CPO (Fig. 6b pole figures; M-index = 0.23), with alignment of $\{001\}$ with lineation, $\{100\}$ perpendicular to foliation, and $\{010\}$ parallel to the Y axis and a non-random MAD.

2.4 Discussion I: ASZ deformation, general flow laws and relative viscosity ratios

In this section, we discuss the evidence for the sequence of deformation events in the ultramafic unit, and the D_3 deformation mechanisms occurring within the different rock units. We use these insights to infer the general flow law characteristics and relative bulk viscosity ratios for the three rock units.

2.4.1 *Strain variations and CPO switch within ultramafics: A signature of deformation sequence*

All of the ultramafic samples display large porphyroclasts with undulose extinction and subgrains surrounded by dynamically recrystallised grains. Assuming that percentage of remnant porphyroclasts (Fig. 8c) can be taken as a proxy for strain (e.g. Rutter and Brodie, 1988; Montési and Hirth, 2003; Svahnberg and Piazzolo, 2010; Platt and Behr, 2011) the sample from the centre of the Anita Ultramafics (AS1309) has experienced the lowest strain, as it has the highest percentage of relict large olivine porphyroclasts (~10 area %; Fig. 8c). By contrast, the sample in the HSZ closest to the Thurso Gneiss (AS1305A2) has the lowest percentage of large porphyroclasts (<1 area %; Fig. 8c), indicating it was subject to the highest strain of the ultramafic samples. The other two HSZ samples, one further from the Thurso Gneiss boundary (AS1306B) and one near the Jagged Gneiss boundary (AS1330) are intermediate to the other samples with similar percentages of large porphyroclasts and intermediate grain sizes (Fig. 8b and c).

Additionally, the ultramafic samples display two distinct CPO fabrics (Fig. 8d). The olivine pole figures for the HSZ samples located close to lithological boundaries (Fig. 7a, b and d) show CPOs consistent with the activity of [100](010) and [001](010) slip systems which corresponds with the CPO fabric type AG (Mainprice, 2015) and the pure shear flow geometry suggested for the D₃ deformation phase (Fig. 8d, Klepeis et al. 1999). By contrast, olivine pole figures for the centre sample (Fig. 7c) show a relatively weak CPO (max = 3.35) with characteristics of a CPO transitional between type C and E (Karato et al., 2008).

We suggest that the C-E type CPO represents a relict CPO from deformation prior to the D₃ event which dominates the HSZs. The larger recrystallised grain size and

higher percentage of relict olivine grains (Figs. 7c; 8b and c) in the centre ultramafic sample indicate a record of little differential stress from the D_3 event and/or it underwent higher temperature of deformation. A C-E type CPO has been suggested to develop at high temperature and intermediate water presence (Karato et al., 2008 and references therein). In addition, Czertowicz et al. (2016b) show that the Anita Ultramafics are highly depleted with $> 30\%$ partial melting which is indicative for a hydrous fore-arc environment. This correlates well with the suggestion by Karato et al. (2008) that extensive melting and type C olivine fabric is expected in the mantle wedge near a subducting slab (Fig. 10b in Karato et al., 2008). In this scenario of C fabric formation, much higher temperatures (> 1000 °C; Kelemen et al., 2004) than those documented for the HSZ D_3 deformation phase (~ 600 °C; Klepeis et al., 1999; Czertowicz et al., 2016c) would be needed. The AG type CPO in the HSZs suggests the relict CPO of the centre was overprinted in the HSZs during the D_3 phase. The observed deflection of the compositional bands causing increasing dip angle of the bands as they approach the HSZ suggests the bands were reoriented during the D_3 deformation phase (Fig. 2a).

Furthermore, the pre- D_3 fabric in the centre of the ultramafic swell agrees with the fact that pre-extension fabrics and geological features can be preserved within the swells of pinch and swell structures, (e.g. Gardner et al. 2016). Our interpretation is consistent with Hill (1995) who found that large portions of the ultramafics represent pre- D_3 features.

2.4.2 *Stress and strain variations within the ultramafics*

Recrystallized grain sizes can be used to infer paleostresses where the smaller the grain size the higher the differential stresses (Twiss 1977). In the field area, samples that are closest to rock unit boundaries, exhibit the smallest recrystallized grain sizes

(Fig. 8b, Table 1). For example, the HSZ ultramafic sample closest to the Thurso Gneiss boundary (AS1305A2; Fig. 7a) has the most extensive recrystallisation to small grains, the smallest recrystallized grain sizes, highest M-index and strongest CPO for olivine and enstatite (Fig. 8a, b and c) of all the ultramafic samples, suggesting it was subjected to the highest differential stress during the D_3 event. This evidence indicates the differential stress from the D_3 event is highest at the layer boundary edge (Fig. 7a), and reduces with distance away from the boundary (Fig. 7b, Fig. 8b), with little evidence of the D_3 deformation event in the centre of the ultramafics as discussed in section 2.4.1.

2.4.3 *Deformation mechanisms*

2.4.3.1 *Anita Ultramafics*

Dislocation creep is interpreted as the dominant regime for olivine in the ultramafic samples investigated as large grains display undulose extinction, have a CPO and SPO close to the lineation, and subgrain boundaries and progressive rotation across the grains (Fig. 7) suggestive of recrystallisation by subgrain rotation (e.g. Urai et al., 1986; Halfpenny et al., 2006, and references therein). The small recrystallised grains, show no internal deformation and lower levels of CPO (Supplementary Fig. 1), thus we interpret minor grain boundary sliding (GBS) to have randomized the CPO inherited from the larger olivine grains (Fliervoet et al., 1999; Jiang et al., 2000; Wheeler et al., 2001), to a varying extent across the ultramafics. GBS can be viewed as a transitional domain where both GBS accommodated by diffusion creep and/or dislocation creep (dis-GBS) can operate (e.g. Hirth and Kohlstedt, 2003; Hansen et al., 2011). The observed grain sizes (Fig. 8b) would, in principle, allow GBS to operate at the ASZ conditions of $\sim 600^\circ\text{C}$ (Hirth and Kohlstedt, 2003; Hansen et al., 2011).

The enstatite grains in the ultramafic samples from areas of medium strain (AS1306B and AS1330; Fig. 7b and d, respectively) have a random SPO and weak CPO. The enstatite grains are more interconnected, forming bands, than in the highest strain sample (Fig. 7a; AS1305A2). There are no relict large enstatite crystals near the boundaries with the gneisses suggesting these have all been recrystallised during the deformation, compared to the centre of the Anita Ultramafics where larger enstatite grains (to several mm) are found. The weak enstatite CPO in these samples can be interpreted as originating from either dislocation creep where the second phase (enstatite) develops a weaker CPO than the main olivine phase (e.g. Cyprych et al. 2016), or GBS was active to some extent and resulted in only a weak CPO (Fliervoet et al., 1999; Jiang et al., 2000; Svahnberg and Piazzolo, 2010; Wheeler et al., 2001). In the highest strain sample (Fig. 7a; AS1305A2), SPO is close to the D₃ lineation and small enstatite grains are dispersed throughout the fine grained olivine. Again, this phase mixing may be due to GBS being active (e.g. Fliervoet et al., 1997; Kruse and Stünitz, 1999; Svahnberg and Piazzolo, 2010).

In summary, in the ultramafics, dislocation creep dominates the pre-D₃ relict olivine and enstatite grains. Syn-D₃ deformation, as seen in the HSZs, is dominated by olivine dislocation creep, with some component of GBS in the fine grained enstatite and recrystallized olivine.

2.4.3.2 Jagged Gneiss and Thurso Gneiss

In the low strain Jagged Gneiss sample, grain sizes (AS1315F; Fig. 5f) are much larger than in the HSZ (Fig. 5e) and show that considerable dynamic recrystallisation to smaller grain sizes has occurred in the HSZ. Plagioclase in the Jagged Gneiss HSZ samples has an M-index of 0.02 (Fig. 6b) with deformation twinning and presence of subgrain boundaries and subgrains of similar size to recrystallised grain

sizes suggesting dislocation creep processes dominated (e.g. Urai et al., 1986; Halfpenny et al., 2006, and references therein). Similarly, quartz displays internal deformation structures indicative of dislocation creep processes such as subgrain boundaries, subgrain sizes similar to recrystallised grain sizes and significant CPO development (Fig. 6b). Hornblende has internal subgrain boundaries indicating that it has also undergone deformation in the dislocation creep regime (Biermann and Van Roermund, 1983). In the Thurso Gneiss, the plagioclase CPO, deformation twinning and subgrain microstructures are very similar to plagioclase in the Jagged Gneiss low strain sample, so here too, we interpreted plagioclase to be dominantly in the dislocation creep regime. Also, quartz displays internal deformation structures indicative of dislocation creep processes such as subgrain boundaries, subgrain sizes similar to recrystallised grain sizes and significant CPO development (Fig. 6a). Biotite in the Thurso Gneiss HSZ sample has internal deformation features, variable grain size, strong SPO parallel to foliation and strong CPO (Fig. 6a, $\max = 10.8$, $M_i = 0.10$). We interpret this to also indicate biotite underwent dominantly dislocation creep.

The scarcity of 120° junctions between grains and absence of foam textures leads us to conclude that there has not been any significant annealing due to post- D_3 high temperatures. In summary, we interpret the gneisses to have undergone D_3 deformation by dislocation creep at amphibolite facies conditions.

2.4.4 *Inferred general flow laws*

During the D_3 event we interpret that both the ultramafics and heterogeneous gneisses have dominantly deformed in the dislocation creep regime, undergoing dynamic recrystallisation to finer grain sizes. Grain size reduction occurred to a variable extent with dominance in the HSZs developed adjacent to the rock unit

boundaries. During the deformation there is evidence for deformation by GBS to variable degrees particularly in the HSZs.

Based on high temperature experimental data, olivine exhibits a stress exponent (n) of 3.5 (Hirth and Kohlstedt, 2003) for the dislocation creep regime, and 2.9 for the dis-GBS regime (Hansen et al., 2011). Whereas, experiments on enstatite suggest a stress exponent between 1 for diffusion creep and 3 for dislocation creep (Bystricky et al., 2016). Based on (a) the presence of enstatite undergoing some GBS (with a stress exponent < 3), and (b) the occurrence of GBS in olivine during the deformation suggesting an n value of < 2.9 (Hansen et al., 2011), we suggest that the ultramafic rocks deformed following a flow regime with a stress exponent of ~ 3 .

We suggest that a stress exponent (n) of 3 is also appropriate for the ortho- and paragneisses in accordance with our observation that these rock types deform dominantly by dislocation creep. The chosen value of 3 is in accordance with the fact that feldspar is one of the main phases accommodating strain in both rock types and experimental data suggests the stress exponent for plagioclase is usually ~ 3 in the dislocation creep regime (Rybacki and Dresen, 2000; Rybacki and Dresen, 2004; Dimanov and Dresen, 2005). Furthermore, since little data is available on the stress exponents for biotite and hornblende deformed in dislocation creep, using the theoretical stress exponent of 3 for this regime (Ranalli, 1995) is appropriate. Even though experimental data for pure quartzite shows a slightly higher stress exponent of 4 (Luan and Paterson, 1992; Hirth et al., 2001), we believe that the overall rheological behaviour is well represented by a stress exponent value of 3, since microstructures suggest quartz does not dominate the strain accommodation.

Based on our field observations, and in conjunction with results from mineral experiments, we conclude that the general flow law for all three pre-D₃ rock units is best described to be non-Newtonian, with an overall stress exponent of 3 (Fig. 8f).

2.4.5 *General relative viscosity inferred from field and experimental data*

The relative bulk viscosity of the rock units can be estimated in general terms from field observations alone. The fact that the ultramafic rocks form a pinch and swell structure indicates the Anita Ultramafics must be more viscous than the surrounding layers (e.g. Smith, 1977; Neurath and Smith, 1982; van der Molen, 1985). The shape asymmetry of the pinch and swell structure with a T_D between 0.090 and 0.103 suggests that the layer is surrounded by dissimilar gneisses on either side (Gardner et al., 2016). The boundary between the Jagged Gneiss and the Anita Ultramafics has lower tortuosity i.e. is straighter than the boundary between the Anita Ultramafics and the Thurso Gneiss (Fig. 1a and 2). Based on models of Gardner et al. (2016) a layer exhibiting a boundary with low tortuosity has a relatively similar strength to the competent layer; hence the Jagged Gneiss, an orthogneiss, is closer in viscosity to the ultramafic unit than the Thurso Gneiss, which exhibits a much more curved and irregular boundary with the Anita Ultramafics.

3 Numerical modelling

The relative rock unit bulk viscosity and the value for the stress exponent of 3 determined from the ASZ field relationships and microstructural analysis (section 2), are used as input parameters for the numerical modelling. Comparison of tortuosity difference measured from the field and calculated in the numerical simulations allows us to determine more precisely the relative viscosity of the three rock units. In

contrast to the models presented by Gardner et al. (2016), the rock units examined here follow general power-law behaviour.

3.1 Numerical model setup

A series of simple three layer models (Fig. 9a) is used to determine the relative effective viscosity of the competent layer to the surrounding layers based on the flow regime ($n = 3$) and tortuosity difference ($T_D \sim 0.1$) values determined for the ASZ pinch and swell structure. The model is set up so that Layer A is the weakest layer, representing the paragneiss, i.e. the Thurso Gneiss. Layer B is the strongest layer and corresponds to the Anita Ultramafics, that is, the competent layer forming the pinch and swell structure. Layer C has intermediate strength and corresponds to the orthogneiss, i.e. the Jagged Gneiss.

This study utilises the numerical setup in Underworld (Moresi et al., 2003; Moresi et al., 2007) as used in Gardner et al. (2015; 2016), with Mohr-Coulomb constituent behaviour defined for the competent central layer. Materials with Mohr-Coulomb constituent behaviour (Edmond and Paterson, 1972; Ord, 1991; Moresi and Mühlhaus, 2006) may exhibit strain localization between grains, in micro-fractures and large-scale features depending on the scale of observation. They have a yield strength, which if exceeded causes the material to fail by localising strain, initially in the orientation plane defined by the friction coefficient. Once localisation occurs, visco-plastic behaviour is modelled with a material softening factor. For this study the friction coefficient (0.6) and material softening (20) values were chosen according to tests performed as part of Gardner et al. (2015) during their modelling of mafic pinch and swells from St Anne Point (Fig. 1a & b). The strain localisation observed with development of thin and thick necks in the St Anne Point mafics is similar to that seen in the ultramafics, and occurs during the same D_3 deformation event, hence at

similar PT conditions. The central layer is defined as an incompressible viscous material. Confining pressure is neglected as all layers of the ASZ are assumed to have been deformed under the same lower to middle continental crust conditions, with no tilting of the package on exhumation. Here, the Mohr-Coulomb constituent behaviour (Ord, 1991; Moresi and Mühlhaus, 2006) is used only to initiate strain localisation, however, there is no explicit modelling of brittle behaviour.

Layers A and C are defined to flow viscously without explicit yield strength. A 2D, constant volume 1 x 1 unit square is subjected to constant extension rate boundary conditions using a horizontal rate of extension equal to -0.5% on the left hand side and +0.5% on the right hand side, with non-periodic, free slip boundaries at the top and bottom to simulate plane strain extension (Fig. 9a). Further details of the model setup are discussed in detail in Gardner et al. (2015; 2016).

The flow behaviour of a layer is defined according to the power-law equation for viscous flow:

$$\dot{\epsilon} = \frac{1}{2\eta} \sigma^n \quad (\text{equation 1})$$

Where $\dot{\epsilon}$ is strain rate, σ is differential stress, n is the stress exponent and η is the viscosity coefficient which reflects the material properties at a specific temperature and pressure in a non-Newtonian material. Dislocation creep dominated flow regime properties, with stress exponent of 3, are chosen to represent the general flow law of the three ASZ units (Fig. 8f).

We define a relative viscosity coefficient ratio of the competent Layer B to Layer A and Layer C, respectively, as:

$$R_{VA} = (\eta_B / \eta_A) \quad (\text{equation 2a})$$

$$R_{VC} = (\eta_B / \eta_C) \quad (\text{equation 2b})$$

Where η is the initial viscosity coefficient of the layer designated by the subscript.

Three series of numerical models are run where R_{VC} is set to 2, 5 and 10. These values were selected as the Anita Ultramafics form asymmetric pinch and swell structures. Based on the relatively straight boundary (low tortuosity value) between ultramafic and orthogneiss (Fig. 1 and 2), the orthogneiss (Layer C) should have a bulk viscosity relatively close to that of the ultramafic. The highly irregular boundary between ultramafic and paragneiss (i.e. Thurso Gneiss), suggests that the paragneiss (Layer A) has significantly lower bulk viscosity relative to the central, most competent layer (Layer B). Consequently, for each R_{VC} , R_{VA} is varied between 10, 20, 40, 80, 160 and 200.

3.2 Results

With progressive stretch, pinch and swell structures develop with strain successfully localizing in neck areas between swells (e.g. Fig. 9b, blue arrow). Where strain is only moderately localized, a thick neck, as defined by Gardner et al. (2015) has formed (Fig. 9b, yellow arrow).

A profile of differential stress taken across a swell at strain of 1.05 and 3.2 in the numerical model (Fig. 9c and d) shows the development of high stress peaks on the edge of a competent layer swell at high stretch. Either side of the Layer B boundary stresses increase towards the boundary. These increased stresses are highest in Layer A close to the Layer B boundary. Stress is lowest in the centre of the swell at higher stretch.

The shape of the pinch and swell structures varies with the varying viscosity coefficient ratios (Fig. 10). When the R_{VC} value is held constant (Fig. 10a, grey lines),

the general trend is for tortuosity difference to increase as R_{VA} increases, that is, as the layer with lowest viscosity coefficient decreases that viscosity coefficient, the tortuosity difference increases. When the R_{VA} value is held constant (Fig. 10a, x axis values) tortuosity difference is highest where R_{VC} is 5. Tortuosity difference is variable for R_{VC} values of 2 and 10, with R_{VC} of 2 higher at an R_{VA} of 20 and 160.

3.3 Discussion 2: Behaviour of layered rock packages at mid-crustal levels – a combined numerical and field based perspective

The numerical models provide insights into the flow behaviour of multi-layered, middle crustal rock packages which can be correlated with the ASZ, New Zealand. These insights are also generally relevant to the behaviour of gneissic rock packages deformed at mid-crustal conditions, corresponding to amphibolite facies conditions.

3.3.1 Stress concentration in a layered rock package

The stress profiles from the numerical model (Fig. 9c and d) show that the competent layer in the ASZ, that is the Anita Ultramafics, should theoretically exhibit increased stress near and at the boundaries with the gneisses later in the D_3 deformation. This corresponds well with the decrease in the percentage of relict grains and decreased recrystallised grain sizes seen on the boundaries of the ultramafic layer (Fig. 8b and c), compared with the ultramafics centre (Layer B), which is interpreted to have largely escaped the D_3 deformation phase.

Confidence in the numerical model is provided by agreement between the model and the field example on (i) the distribution of stress at higher stretch values, and (ii) the occurrence in the model of both necks and thick necks as seen in the field example (Fig. 1a, 9b, blue and yellow arrows).

3.3.2 Prediction of relative and bulk viscosity for ASZ lithologies

The tortuosity difference for the Anita Ultramafics in the ASZ was determined to be ~ 0.1 , based on the measurements made from the inferred boundaries (Figs. 1a and 2b) with ~ 0.090 and ~ 0.103 for T_{D1} and T_{D2} , respectively. Comparing this with the tortuosity difference for the three numerical model series (Fig. 10a) suggests that the model with $R_{VC} = 5$ and $R_{VA} = 80$ represents the closest match to the ASZ. However, within error, $R_{VA} = 50$ to 150 , and $R_{VC} = 2$ to 5 .

It is possible to determine an approximate bulk viscosity of each rock unit in the field example using calculations based on the experimentally determined viscosity for olivine as an approximation of the bulk viscosity of the ultramafic unit combined with the relative effective viscosities determined by the numerical modelling. However, it should be noted that these calculations are only accurate to the first order due to significant uncertainties in the input values. In addition, for laboratory derived flow laws, a constant strain rate is assumed. The viscosity for olivine can be calculated using equation 3, (from Hirth and Kohlstedt, 2003) assuming no melt, wet conditions and grain size independent dislocation creep as supported by the quantitative microstructural analysis:

$$\dot{\epsilon} = A \sigma^n f_{H_2O}^r \exp\left(-\frac{E^* + PV^*}{RT}\right) \quad (\text{equation 3})$$

where $\dot{\epsilon}$ is strain rate (s^{-1}), A is a material constant ($MPa^{-n-r} \mu m^p/s$), σ is differential stress (MPa), n is the stress exponent, f_{H_2O} is water fugacity (MPa), r is water fugacity exponent, E^* is the activation energy (J/mol), V^* is the activation volume (m^3/mol), P is pressure (Pa), T is temperature ($^{\circ}K$) and R is the gas constant ($J/^{\circ}K.mol$). Strain rate for the middle crust has been shown to be in the range of 10^{-13} to $10^{-17} s^{-1}$ (Pfiffner and Ramsay, 1982; Prior et al., 1990). Assuming a strain rate of

10^{-14} s^{-1} , which allows for localisation (Pfiffner and Ramsay, 1982) in the ultramafic layer, and utilizing the additional values from the literature (Table 2), differential stress is determined by rearranging equation 3. Accordingly, it is $\sim 600 \text{ MPa}$. Viscosity is calculated using $0.5 \times (\text{stress}/\text{strain rate})$, which gives a bulk viscosity for the ultramafics of $\sim 3.0 \times 10^{22} \text{ Pa s}$. Using the effective viscosity ratios determined by a profile of effective viscosity across the numerical model at a stretch of 1 (Supplementary Figure 2) suggests the bulk viscosity prior to the onset of deformation of the orthogneiss is ~ 1.7 times weaker at $1.7 \times 10^{22} \text{ Pa s}$ and the paragneiss is ~ 4.3 times weaker at $6.9 \times 10^{21} \text{ Pa s}$ than the ultramafics. Similarly, the effective viscosity profile across a swell at a stretch of 2.3 (Supplementary Figure 2) indicates the bulk viscosity during the deformation of the orthogneiss is ~ 13 times weaker at $2.3 \times 10^{21} \text{ Pa s}$, and the paragneiss is ~ 32 times weaker at $9.4 \times 10^{20} \text{ Pa s}$, than the ultramafics. From the literature the bulk viscosity for the middle crust has a wide range between 10^{16} and 10^{21} Pa s (Kirby, 1983; Carter and Tsenn, 1987; Evans and Kohlstedt, 1995; Clark and Royden, 2000; Vergnolle et al., 2003; Johnson et al., 2007; Yamasaki and Houseman, 2012), with lower continental crust in the upper part of this range from 10^{18} to 10^{21} (e.g. Bürgmann and Dresen, 2008, and references therein). Bürgmann and Dresen (2008) also show in their summary of geodetic measurements obtained from earthquakes and lake level fluctuations, that transient viscosity reduction due to relaxation caused by a deformation event can cause viscosities up to two orders of magnitude lower than the steady state viscosity. This correlates well with the bulk viscosity values determined here for the pre-deformation kilometre-scale rock units which equate to the higher steady state viscosities, while the syn-deformation viscosities for the gneisses which are one to two orders of magnitude weaker.

Applying a similar methodology using published flow laws for wet anorthite, Gardner et al. (2016) found, in a localized outcrop-scale shear zone, a plagioclase-rich layer to have a viscosity of $\sim 1.1 \times 10^{17}$ Pa s and a gabbroic gneiss to have a viscosity range of 2.8×10^{15} to 1.1×10^{16} Pa s. These values are orders of magnitude lower than the values determined here. This is not surprising, as those rocks deformed by Newtonian flow, which results in a general decrease in bulk viscosity relative to the same rock deforming by non-Newtonian flow (e.g. Frost and Ashby, 1972; Smith et al. 2015). Anorthite is commonly used in numerical models as a proxy for the middle continental crust (e.g. Weinberg et al., 2007; Rosenbaum et al., 2010; Brune et al., 2014; Erdős et al., 2014). Based on experimental values for dry anorthite (after Rybacki and Dresen, 2004) and assuming a strain rate of 10^{-14} s^{-1} we can calculate stress to be ~ 37 MPa and viscosity 1.8×10^{21} Pa (using equation 3, ASZ conditions and values in table 2). This calculated viscosity compares well with our results as it is between the values calculated here for the paragneiss and orthogneiss.

3.3.3 *Prediction of relative and absolute bulk viscosity of km-scale rock units*

Due to uncertainties in outcrop shape (tortuosity) derived from natural outcrops, and the necessary assumptions for n values, the method presented here provides a first order estimate of the bulk viscosity only. The user may need to adjust tortuosity measurements taking possible non-vertical rock unit boundaries into account. Furthermore, our method should only be applied in situations where the thickness of the rock units does not exceed several km, as otherwise gravitational effects may become important. However, it can be used in conjunction with other geometric treatments (e.g. Schmalholz et al., 2002).

The new tool presented is important as, in most cases, the generalized properties needed for large-scale geotectonic models are extrapolated from laboratory data for

the properties of mainly monomineralic rock types, such as dunite, quartzite and pure plagioclase rock (e.g. Strehlau and Meissner, 1987; Beaumont et al., 2001; Weinberg et al., 2007; Rosenbaum et al., 2010; Brune et al., 2014). However, it is clear that this is not adequate (Bürgmann and Dresen, 2008; Gardner et al., 2016).

Here we show that, if it is possible to quantify the boundary shape between different rock units by measuring the boundary tortuosity, this tortuosity can be used to derive the relative bulk viscosities appropriate for modelling of kilometre- to 100s of kilometre-scale structures. These bulk viscosities are independent of the possible smaller scale heterogeneities within each rock unit. Importantly, the method presented is one of the few methods that can be used in very remote areas, where rock unit boundary shapes can be determined utilising the ever increasing availability of high quality satellite and geophysical data.

In addition to relative bulk viscosity data, it is possible to derive absolute bulk viscosity values if stresses and strain rates are known. It should be noted though, that even without the derivation of absolute values, the more accurate determination of relative bulk viscosities represents an important step towards more reliable geodynamic models.

4 CONCLUSIONS

The Anita Ultramafics in the ASZ is an example of a kilometre-scale pinch and swell structure with asymmetric shape parallel to the elongation or stretch direction. While we conducted a combined field and numerical study on the ASZ deformed at mid-crustal levels, the tool developed and applied in this study, can be more generally utilised to determine relative and absolute bulk viscosities of rock units involved in multilayer deformation. Importantly, using kilometre-scale shape variations allows the

derivation of bulk viscosity for rock units that may be heterogeneous at the mm to 10m scale, but have deformed near homogeneously at the kilometre or tens of kilometre scale.

We conclude that the shape characteristics of kilometre-scale pinch and swell structures allows the determination of valid values for relative and absolute bulk viscosity at the rock unit scale, even where heterogeneity occurs within each rock unit at the centimetre to metre scale. Our analysis shows that during deformation at mid-crustal conditions, paragneisses can be thirty times less viscous than an ultramafic unit, whereas orthogneisses have intermediate viscosity, approximately a thirteenth of the ultramafics, and up to three times greater than the paragneisses. At an assumed strain rate of 10^{-14} s^{-1} and mid crustal conditions the viscosity of typical harzburgitic ultramafic layers undergoing deformation is $3.0 \times 10^{22} \text{ Pa s}$, with orthogneiss being approximately 13 times less viscous at $2.3 \times 10^{21} \text{ Pa s}$ and heterogeneous paragneiss approximately 32 times weaker at $9.4 \times 10^{20} \text{ Pa s}$.

During deformation in non-Newtonian flow, general shape properties are similar to those seen by Gardner et al. (2016) in Newtonian flow where: (i) the highest tortuosity boundary of the pinch and swell is the boundary with the weakest geological unit, and (ii) the lowest tortuosity boundary of the pinch and swell structures is the boundary with the stronger geological unit. In addition, the highest stresses are at the boundary of the most competent layer with the weakest geological unit and stress reduces with distance from the units' boundary.

Our study shows that the synergy of fieldwork, petrography, quantitative microstructural analysis, and numerical modelling provides powerful insights into crustal rheologies. We find the methodology of Gardner et al. (2016), using shape symmetry/asymmetry of the pinch and swell structure, can be extended to kilometre-

scale pinch and swell structures undergoing non-Newtonian flow regimes, and provides a gauge for the relative bulk strength of the rock units in the package. Application of this new tool is expected to allow additional refinement of the appropriate flow properties, vital for reliable, large-scale geotectonic models.

5 ACKNOWLEDGEMENTS

Logistical and analytical funding was provided by an MQRes scholarship (RG), Future Fellowship (FT1101100070 to SP) and internal funding from the Department of Earth and Planetary Sciences, Macquarie University. Code development in Underworld was supported by the Victorian Partnership for Advanced Computing and Monash University (Moresi et al., 2003; Moresi et al., 2007). We thank the Department of Conservation in Te Anau for permission to visit and sample localities within Anita Shear Zone, Fiordland National Park and Bruce Hobbs for his comments on the manuscript. The authors would also like to thank Laurent Montési, Michael Stipp and Marta Adamuszek for their careful and constructive reviews, and Zheng-Xiang Li for editorial handling. This is contribution xxx from the ARC Centre of Excellence for Core to Crust Fluid Systems (<http://www.cafs.mq.edu.au>) and xxx in the GEMOC Key Centre (<http://www.gemoc.mq.edu.au>).

6 REFERENCES

- Abe, S., Urai, J.L., 2012. Discrete element modeling of boudinage: Insights on rock rheology, matrix flow, and evolution of geometry. *Journal of Geophysical Research: Solid Earth* 117, B01407.
- Barr, T.D., Houseman, G.A., 1996. Deformation fields around a fault embedded in a non-linear ductile medium. *Geophysical Journal International* 125, 473-490.
- Beaumont, C., Jamieson, R.A., Nguyen, M.H., Lee, B., 2001. Himalayan tectonics explained by extrusion of a low-viscosity crustal channel coupled to focused surface denudation. *Nature* 414, 738-742.

- Bestmann, M., Prior, D.J., 2003. Intragranular dynamic recrystallization in naturally deformed calcite marble: diffusion accommodated grain boundary sliding as a result of subgrain rotation recrystallization. *Journal of Structural Geology* 25, 1597-1613.
- Biermann, C., Van Roermund, H.L.M., 1983. Defect structures in naturally deformed clin amphiboles—a TEM study. *Tectonophysics* 95, 267-278.
- Brace, W.F., Kohlstedt, D.L., 1980. Limits on lithospheric stress imposed by laboratory experiments. *Journal of Geophysical Research: Solid Earth* 85, 6248-6252.
- Bradshaw, J.Y., 1990. Geology of crystalline rocks of northern Fiordland: Details of the granulite facies Western Fiordland Orthogneiss and associated rock units. *New Zealand Journal of Geology and Geophysics* 33, 465-484.
- Bruijn, R.H.C., Skemer, P., 2014. Grain-size sensitive rheology of orthopyroxene. *Geophysical Research Letters* 41, 4894-4903.
- Brune, S., Heine, C., Pérez-Gussinyé, M., Sobolev, S.V., 2014. Rift migration explains continental margin asymmetry and crustal hyper-extension. *Nat Commun* 5.
- Bürgmann, R., Dresen, G., 2008. Rheology of the Lower Crust and Upper Mantle: Evidence from Rock Mechanics, Geodesy, and Field Observations. *Annual Review of Earth and Planetary Sciences* 36, 531-567.
- Bystricky, M., Lawlis, J., Mackwell, S., Heidelbach, F., Raterron, P., 2016. High-temperature deformation of enstatite aggregates. *Journal of Geophysical Research: Solid Earth* 121, 6384-6400.
- Carter, N.L., Tsenn, M.C., 1987. Flow properties of continental lithosphere. *Tectonophysics* 136, 27-63.
- Clark, M.K., Royden, L.H., 2000. Topographic ooze: Building the eastern margin of Tibet by lower crustal flow. *Geology* 28, 703-706.
- Clarke, G.L., Klepeis, K.A., Daczko, N.R., 2000. Cretaceous high-P granulites at Milford Sound, New Zealand: metamorphic history and emplacement in a convergent margin setting. *Journal of Metamorphic Geology* 18, 359-374.
- Cloos, E., 1947. Boudinage. *Eos, Transactions American Geophysical Union* 28, 626-632.
- Cyprych, D., Piazzolo, S., Wilson, C.J.L., Luzin, V., Prior, D.J., 2016. Rheology, microstructure and crystallographic preferred orientation of matrix containing a dispersed second phase: Insight from experimentally deformed ice. *Earth and Planetary Science Letters* 449, 272-281.
- Czertowicz, T.A., Scott, J.M., Piazzolo, S., 2016a. Coupled extrusion of sub-arc lithospheric mantle and lower crust during orogen collapse: a case study from Fiordland, New Zealand. *Journal of Metamorphic Geology*, n/a-n/a.
- Czertowicz, T.A., Scott, J.M., Waight, T.E., Palin, J.M., Van der Meer, Q.H.A., Le Roux, P., Münker, C., Piazzolo, S., 2016b. The Anita Peridotite, New Zealand: Ultra-depletion and Subtle Enrichment in Sub-arc Mantle. *Journal of Petrology*.
- Czertowicz, T.A., Toy, V.G., Scott, J.M., 2016c. Recrystallisation, phase mixing and strain localisation in peridotite during rapid extrusion of sub-arc mantle lithosphere. *Journal of Structural Geology* 88, 1-19.
- Dahlen, F., 1984. Noncohesive critical Coulomb wedges: An exact solution. *Journal of Geophysical Research: Solid Earth (1978–2012)* 89, 10125-10133.
- de Ronde, A.A., Stünitz, H., Tullis, J., Heilbronner, R., 2005. Reaction-induced weakening of plagioclase–olivine composites. *Tectonophysics* 409, 85-106.
- Dell'Angelo, L.N., Tullis, J., 1989. Fabric development in experimentally sheared quartzites. *Tectonophysics* 169, 1-21.

- Dell'Angelo, L.N., Tullis, J., 1996. Textural and mechanical evolution with progressive strain in experimentally deformed aplite. *Tectonophysics* 256, 57-82.
- Dimanov, A., Dresen, G., 2005. Rheology of synthetic anorthite-diopside aggregates: Implications for ductile shear zones. *Journal of Geophysical Research: Solid Earth* 110, B07203.
- Edmond, J.M., Paterson, M.S., 1972. Volume changes during the deformation of rocks at high pressures. *International Journal of Rock Mechanics and Mining Sciences & Geomechanics Abstracts* 9, 161-182.
- Erdős, Z., Huismans, R.S., van der Beek, P., Thieulot, C., 2014. Extensional inheritance and surface processes as controlling factors of mountain belt structure. *Journal of Geophysical Research: Solid Earth* 119, 9042-9061.
- Evans, B., Kohlstedt, D.L., 1995. Rheology of Rocks, *Rock Physics & Phase Relations*. American Geophysical Union, pp. 148-165.
- Farla, R.J.M., Karato, S.-i., Cai, Z., 2013. Role of orthopyroxene in rheological weakening of the lithosphere via dynamic recrystallization. *Proceedings of the National Academy of Sciences* 110, 16355-16360.
- Fliervoet, T.F., Drury, M.R., Chopra, P.N., 1999. Crystallographic preferred orientations and misorientations in some olivine rocks deformed by diffusion or dislocation creep. *Tectonophysics* 303, 1-27.
- Fliervoet, T.F., White, S.H., Drury, M.R., 1997. Evidence for dominant grain-boundary sliding deformation in greenschist- and amphibolite-grade polymineralic ultramylonites from the Redbank Deformed Zone, Central Australia. *Journal of Structural Geology* 19, 1495-1520.
- Frehner, M., Reif, D., Grasemann, B., 2012. Mechanical versus kinematical shortening reconstructions of the Zagros High Folded Zone (Kurdistan region of Iraq). *Tectonics* 31, n/a-n/a.
- Frost, H., Ashby, M., 1972. Deformation-Mechanism Maps and the Creep of Tungsten Lamp Filaments. DTIC Document.
- Gardner, R.L., Piazzolo, S., Daczko, N.R., 2015. Pinch and swell structures: evidence for strain localisation by brittle–viscous behaviour in the middle crust. *Solid Earth* 6, 1045-1061.
- Gardner, R.L., Piazzolo, S., Daczko, N.R., 2016. Shape of pinch and swell structures as a viscosity indicator: Application to lower crustal polyphase rocks. *Journal of Structural Geology* 88, 32-45.
- Gleason, G.C., Tullis, J., 1995. A flow law for dislocation creep of quartz aggregates determined with the molten salt cell. *Tectonophysics* 247, 1-23.
- Goldstein, A.G., 1988. Factors affecting the kinematic interpretation of asymmetric boudinage in shear zones. *Journal of Structural Geology* 10, 707-715.
- Google Earth, 2016 "Milford Sound, New Zealand", Imagery ©2016 DigitalGlobe, TerraMetrics, Map data ©2016, Google, <https://www.google.com.au/maps/place/Milford+Sound/@-44.6209913,167.7340484,11033m/data=!3m1!1e3!4m5!3m4!1s0xa9d5e04dba4b49e1:0x2a00ef86ab64de00!8m2!3d-44.6414024!4d167.8973801>. (15Aug2016).
- Gresens, R.L., 1966. The Effect of Structurally Produced Pressure Gradients on Diffusion in Rocks. *The Journal of Geology* 74, 307-321.
- Groome, W.G., Koons, P.O., Johnson, S.E., 2008. Metamorphism, transient mid-crustal rheology, strain localization and the exhumation of high-grade metamorphic rocks. *Tectonics* 27, n/a-n/a.
- Gueydan, F., Précigout, J., 2014. Modes of continental rifting as a function of ductile strain localization in the lithospheric mantle. *Tectonophysics* 612–613, 18-25.

- Halfpenny, A., Prior, D.J., Wheeler, J., 2006. Analysis of dynamic recrystallization and nucleation in a quartzite mylonite. *Tectonophysics* 427, 3-14.
- Handy, M.R., 1990. The solid-state flow of polymineralic rocks. *Journal of Geophysical Research: Solid Earth* 95, 8647-8661.
- Handy, M.R., 1994. Flow laws for rocks containing two non-linear viscous phases: A phenomenological approach. *Journal of Structural Geology* 16, 287-301.
- Hansen, L.N., Warren, J.M., 2015. Quantifying the effect of pyroxene on deformation of peridotite in a natural shear zone. *Journal of Geophysical Research: Solid Earth* 120, 2717-2738.
- Hansen, L.N., Zimmerman, M.E., Kohlstedt, D.L., 2011. Grain boundary sliding in San Carlos olivine: Flow law parameters and crystallographic-preferred orientation. *Journal of Geophysical Research: Solid Earth* 116, B08201.
- Herwegh, M., Linckens, J., Ebert, A., Berger, A., Brodhag, S.H., 2011. The role of second phases for controlling microstructural evolution in polymineralic rocks: A review. *Journal of Structural Geology* 33, 1728-1750.
- Herwegh, M., Xiao, X., Evans, B., 2003. The effect of dissolved magnesium on diffusion creep in calcite. *Earth and Planetary Science Letters* 212, 457-470.
- Hill, E.J., 1995. A deep crustal shear zone exposed in western Fiordland, New Zealand. *Tectonics* 14, 1172-1181.
- Hirth, G., Kohlstedt, D., 2003. Rheology of the Upper Mantle and the Mantle Wedge: A View from the Experimentalists, Inside the Subduction Factory. *American Geophysical Union*, pp. 83-105.
- Hirth, G., Teyssier, C., Dunlap, J.W., 2001. An evaluation of quartzite flow laws based on comparisons between experimentally and naturally deformed rocks. *Int J Earth Sci (Geol Rundsch)* 90, 77-87.
- Hobbs, B., Regenauer-Lieb, K., Ord, A., 2008. Folding with thermal–mechanical feedback. *Journal of Structural Geology* 30, 1572-1592.
- Hollis, J.A., Clarke, G.L., Klepeis, K.A., Daczko, N.R., Ireland, T.R., 2003. Geochronology and geochemistry of high-pressure granulites of the Arthur River Complex, Fiordland, New Zealand: Cretaceous magmatism and metamorphism on the palaeo-Pacific Margin. *Journal of Metamorphic Geology* 21, 299-313.
- Holyoke III, C.W., Tullis, J., 2006a. The interaction between reaction and deformation: an experimental study using a biotite + plagioclase + quartz gneiss. *Journal of Metamorphic Geology* 24, 743-762.
- Holyoke III, C.W., Tullis, J., 2006b. Mechanisms of weak phase interconnection and the effects of phase strength contrast on fabric development. *Journal of Structural Geology* 28, 621-640.
- Ireland, T.R., Gibson, G.M., 1998. SHRIMP monazite and zircon geochronology of high-grade metamorphism in New Zealand. *Journal of Metamorphic Geology* 16, 149.
- Ji, S., 2004. A generalized mixture rule for estimating the viscosity of solid-liquid suspensions and mechanical properties of polyphase rocks and composite materials. *Journal of Geophysical Research: Solid Earth* 109, n/a-n/a.
- Jiang, Z., Prior, D.J., Wheeler, J., 2000. Albite crystallographic preferred orientation and grain misorientation distribution in a low-grade mylonite: implications for granular flow. *Journal of Structural Geology* 22, 1663-1674.
- Johnson, K.M., Hilley, G.E., Bürgmann, R., 2007. Influence of lithosphere viscosity structure on estimates of fault slip rate in the Mojave region of the San Andreas fault system. *Journal of Geophysical Research: Solid Earth* 112, n/a-n/a.

- Jordan, P.G., 1987. The deformational behaviour of biminerale limestone-halite aggregates. *Tectonophysics* 135, 185-197.
- Karato, S.-i., Jung, H., Katayama, I., Skemer, P., 2008. Geodynamic Significance of Seismic Anisotropy of the Upper Mantle: New Insights from Laboratory Studies. *Annual Review of Earth and Planetary Sciences* 36, 59-95.
- Kelemen, P.B., Rilling, J.L., Parmentier, E.M., Mehl, L., Hacker, B.R., 2004. Thermal Structure due to Solid-State Flow in the Mantle Wedge Beneath Arcs, Inside the Subduction Factory. *American Geophysical Union*, pp. 293-311.
- Kenkmann, T., Dresen, G., 1998. Structures and Properties of High Strain Zones in Rocks Stress gradients around porphyroclasts: palaeopiezometric estimates and numerical modelling. *Journal of Structural Geology* 20, 163-173.
- Kirby, S.H., 1983. Rheology of the lithosphere. *Reviews of Geophysics* 21, 1458-1487.
- Klepeis, K.A., Daczko, N.R., Clarke, G.L., 1999. Kinematic vorticity and tectonic significance of superposed mylonites in a major lower crustal shear zone, northern Fiordland, New Zealand. *Journal of Structural Geology* 21, 1385-1405.
- Kobberger, G., Zulauf, G., 1995. Experimental folding and boudinage under pure constrictional conditions. *Journal of Structural Geology* 17, 1055-1063.
- Komoróczy, A., Abe, S., Urai, J., 2013. Meshless numerical modeling of brittle–viscous deformation: first results on boudinage and hydrofracturing using a coupling of discrete element method (DEM) and smoothed particle hydrodynamics (SPH). *Comput Geosci* 17, 373-390.
- Kruse, R., Stünitz, H., 1999. Deformation mechanisms and phase distribution in mafic high-temperature mylonites from the Jotun Nappe, southern Norway. *Tectonophysics* 303, 223-249.
- Llorens, M.-G., Bons, P.D., Giera, A., Gomez-Rivas, E., 2013. When do folds unfold during progressive shear? *Geology* 41, 563-566.
- Lohest, M., Stainier, X., Fourmarier, P., 1908. Compte rendu de la session extraordinaire de la Société géologique de Belgique, tenue à Eupen et Bastogne les 29, 30 et 31 août et le 1, 2 et 3 Septembre 1908. *Annales de la Société géologique de Belgique* 36, 275-282.
- Luan, F.C., Paterson, M.S., 1992. Preparation and deformation of synthetic aggregates of quartz. *Journal of Geophysical Research: Solid Earth* 97, 301-320.
- Mainprice, D., 2015. Seismic anisotropy of the deep earth from a mineral and rock physics perspective, in: Schubert, G. (Ed.), *Treatise on Geophysics*. Elsevier, Oxford, pp. 487-538.
- Mainprice, D., Bachmann, F., Hielscher, R., Schaeben, H., 2015. Descriptive tools for the analysis of texture projects with large datasets using MTEX: strength, symmetry and components. *Geological Society, London, Special Publications* 409, 251-271.
- Mengong, M.E., Zulauf, G., 2006. Coeval folding and boudinage under plane strain with the axis of no change perpendicular to the layer. *Int J Earth Sci (Geol Rundsch)* 95, 178-188.
- Molnar, P., 1992. Chapter 18 Brace-Goetze Strength Profiles, The Partitioning of Strike-slip and Thrust Faulting at Zones of Oblique Convergence, and the Stress-Heat Flow Paradox of the San Andreas Fault, in: Brian, E., Teng-fong, W. (Eds.), *International Geophysics*. Academic Press, pp. 435-459.
- Montési, L.G.J., Hirth, G., 2003. Grain size evolution and the rheology of ductile shear zones: from laboratory experiments to postseismic creep. *Earth and Planetary Science Letters* 211, 97-110.

- Moresi, L., Dufour, F., Mühlhaus, H.B., 2003. A Lagrangian integration point finite element method for large deformation modeling of viscoelastic geomaterials. *Journal of Computational Physics* 184, 476-497.
- Moresi, L., Mühlhaus, H.B., 2006. Anisotropic viscous models of large-deformation Mohr–Coulomb failure. *Philosophical Magazine* 86, 3287-3305.
- Moresi, L., Quenette, S., Lemiale, V., Mériaux, C., Appelbe, B., Mühlhaus, H.B., 2007. Computational approaches to studying non-linear dynamics of the crust and mantle. *Physics of the Earth and Planetary Interiors* 163, 69-82.
- Neurath, C., Smith, R.B., 1982. The effect of material properties on growth rates of folding and boudinage: Experiments with wax models. *Journal of Structural Geology* 4, 215-229.
- Nishihara, Y., Ohuchi, T., Kawazoe, T., Spengler, D., Tasaka, M., Kikegawa, T., Suzuki, A., Ohtani, E., 2014. Rheology of fine-grained forsterite aggregate at deep upper mantle conditions. *Journal of Geophysical Research: Solid Earth* 119, 2013JB010473.
- Nutman, A.P., Friend, C.R.L., 2009. New 1:20,000 scale geological maps, synthesis and history of investigation of the Isua supracrustal belt and adjacent orthogneisses, southern West Greenland: A glimpse of Eoarchaeon crust formation and orogeny. *Precambrian Research* 172, 189-211.
- Ord, A., 1991. Deformation of rock: A pressure-sensitive, dilatant material. *PAGEOPH* 137, 337-366.
- Pfiffner, O.A., Ramsay, J.G., 1982. Constraints on geological strain rates: Arguments from finite strain states of naturally deformed rocks. *Journal of Geophysical Research: Solid Earth* 87, 311-321.
- Piazolo, S., Bestmann, M., Prior, D.J., Spiers, C.J., 2006. Temperature dependent grain boundary migration in deformed-then-annealed material: Observations from experimentally deformed synthetic rocksalt. *Tectonophysics* 427, 55-71.
- Platt, J.P., Behr, W.M., 2011. Grain size evolution in ductile shear zones: Implications for strain localization and the strength of the lithosphere. *Journal of Structural Geology* 33, 537-550.
- Prior, D.J., Knipe, R.J., Handy, M.R., 1990. Estimates of the rates of microstructural changes in mylonites. *Geological Society, London, Special Publications* 54, 309-319.
- Prior, D.J., Wheeler, J., Peruzzo, L., Spiess, R., Storey, C., 2002. Some garnet microstructures: an illustration of the potential of orientation maps and misorientation analysis in microstructural studies. *Journal of Structural Geology* 24, 999-1011.
- Ramberg, H., 1955. Natural and Experimental Boudinage and Pinch-and-Swell Structures. *The Journal of Geology* 63, 512-526.
- Ramsay, J.G., 1980. Shear zone geometry: A review. *Journal of Structural Geology* 2, 83-99.
- Ramsay, J.G., Graham, R.H., 1970. Strain variation in shear belts. *Canadian Journal of Earth Sciences* 7, 786-813.
- Rasband, W.S., 2013. ImageJ, U. S. National Institutes of Health, Bethesda, Maryland, USA, <http://imagej.nih.gov/ij/>. (15Aug2016).
- Ranalli, G., 1995. *Rheology of the Earth*, 2nd ed. Chapman & Hall, London, UK.
- Regenauer-Lieb, K., Poulet, T., Siret, D., Fousseis, F., Liu, J., Gessner, K., Gaede, O., Morra, G., Hobbs, B.E., Ord, A., Mühlhaus, H., Yuen, D.A., Weinberg, R.F., Rosenbaum, G., 2009. First steps towards modeling a multi-scale earth system, in: Xing, H. (Ed.), *Advances in Geocomputing*. Springer Berlin Heidelberg.

- Rennie, S.F., Fagereng, Å., Diener, J.F.A., 2013. Strain distribution within a km-scale, mid-crustal shear zone: The Kuckaus Mylonite Zone, Namibia. *Journal of Structural Geology* 56, 57-69.
- Reuss, A. (1929). "Berechnung der Fließgrenze von Mischkristallen auf Grund der Plastizitätsbedingung für Einkristalle". *Zeitschrift für Angewandte Mathematik und Mechanik* 9: 49–58. doi:10.1002/zamm.19290090104
- Rey, P.F., Muller, R.D., 2010. Fragmentation of active continental plate margins owing to the buoyancy of the mantle wedge. *Nature Geosci* 3, 257-261.
- Rey, P.F., Teyssier, C., Kruckenberg, S.C., Whitney, D.L., 2011. Viscous collision in channel explains double domes in metamorphic core complexes. *Geology* 39, 387-390.
- Rey, P.F., Teyssier, C., Whitney, D.L., 2010. Limit of channel flow in orogenic plateaux. *Lithosphere* 2, 328-332.
- Roberts, E.A., Houseman, G.A., 2001. Geodynamics of central Australia during the intraplate Alice Springs Orogeny: thin viscous sheet models. Geological Society, London, Special Publications 184, 139-164.
- Rosenbaum, G., Regenauer-Lieb, K., Weinberg, R.F., 2010. Interaction between mantle and crustal detachments: A nonlinear system controlling lithospheric extension. *Journal of Geophysical Research: Solid Earth* 115, B11412.
- Rutter, E.H., Brodie, K.H., 1988. The role of tectonic grain size reduction in the rheological stratification of the lithosphere. *Geol Rundsch* 77, 295-307.
- Rybacki, E., Dresen, G., 2000. Dislocation and diffusion creep of synthetic anorthite aggregates. *Journal of Geophysical Research: Solid Earth* 105, 26017-26036.
- Rybacki, E., Dresen, G., 2004. Deformation mechanism maps for feldspar rocks. *Tectonophysics* 382, 173-187.
- Schmalholz, S.M., Maeder, X., 2012. Pinch-and-swell structure and shear zones in viscoplastic layers. *Journal of Structural Geology* 37, 75-88.
- Schmalholz, S.M., Podladchikov, Y.Y., Burg, J.P., 2002. Control of folding by gravity and matrix thickness: Implications for large-scale folding. *Journal of Geophysical Research: Solid Earth* 107, ETG 1-1-ETG 1-16.
- Schmalholz, S.M., Schmid, D.W., Fletcher, R.C., 2008. Evolution of pinch-and-swell structures in a power-law layer. *Journal of Structural Geology* 30, 649-663.
- Shea, W.T., Kronenberg, A.K., 1993. Strength and anisotropy of foliated rocks with varied mica contents. *Journal of Structural Geology* 15, 1097-1121.
- Skemer, P., Katayama, I., Jiang, Z., Karato, S.-i., 2005. The misorientation index: Development of a new method for calculating the strength of lattice-preferred orientation. *Tectonophysics* 411, 157-167.
- Smith, R.B., 1975. Unified theory of the onset of folding, boudinage, and mullion structure. *Geological Society of America Bulletin* 86, 1601-1609.
- Smith, R.B., 1977. Formation of folds, boudinage, and mullions in non-Newtonian materials. *Geological Society of America Bulletin* 88, 312-320.
- Strehlau, J., Meissner, R., 1987. Estimation of Crustal Viscosities and Shear Stresses from an Extrapolation of Experimental Steady State Flow Data, in: Fuchs, K., Froidevaux, C. (Eds.), *Composition, Structure and Dynamics of the Lithosphere-Asthenosphere System*. American Geophysical Union, Washington, D.C., pp. 69-87.
- Stuart-Smith, P.G., 1990. The emplacement and fault history of the Coolac Serpentine, Lachlan Fold Belt, southeastern Australia. *Journal of Structural Geology* 12, 621-638.
- Stünitz, H., Fitz Gerald, J.D., 1993. Deformation of granitoids at low metamorphic grade. II: Granular flow in albite-rich mylonites. *Tectonophysics* 221, 299-324.

- Svahnberg, H., Piazzolo, S., 2010. The initiation of strain localisation in plagioclase-rich rocks: Insights from detailed microstructural analyses. *Journal of Structural Geology* 32, 1404-1416.
- Tasaka, M., Hiraga, T., 2013. Influence of mineral fraction on the rheological properties of forsterite + enstatite during grain-size-sensitive creep: 1. Grain size and grain growth laws. *Journal of Geophysical Research: Solid Earth* 118, 3970-3990.
- Tasaka, M., Hiraga, T., Michibayashi, K., 2014. Influence of mineral fraction on the rheological properties of forsterite + enstatite during grain size sensitive creep: 3. Application of grain growth and flow laws on peridotite ultramylonite. *Journal of Geophysical Research: Solid Earth* 119, 840-857.
- Tetley, M.G., Daczko, N.R., 2014. Virtual Petrographic Microscope: a multi-platform education and research software tool to analyse rock thin-sections. *Australian Journal of Earth Sciences* 61, 631-637.
- Tikoff, B., Fossen, H., 1995. The limitations of three-dimensional kinematic vorticity analysis. *Journal of Structural Geology* 17, 1771-1784.
- Tikoff, B., Teysier, C., Waters, C., 2002. Clutch tectonics and the partial attachment of lithospheric layers. *EGU Stephan Mueller Special Publication Series* 1, 57-73.
- Tommasi, A., Mainprice, D., Canova, G., Chastel, Y., 2000. Viscoplastic self-consistent and equilibrium-based modeling of olivine lattice preferred orientations: Implications for the upper mantle seismic anisotropy. *Journal of Geophysical Research: Solid Earth* 105, 7893-7908.
- Tulloch, A., Ireland, T., Kimbrough, D., Griffin, W., Ramezani, J., 2011. Autochthonous inheritance of zircon through Cretaceous partial melting of Carboniferous plutons: the Arthur River Complex, Fiordland, New Zealand. *Contrib Mineral Petrol* 161, 401-421.
- Turnbull, I.M., Allibone, A.H., Jongens, R., 2010. Geology of the Fiordland area: scale 1:250,000. Institute of Geological & Nuclear Sciences, Lower Hutt.
- Twiss, R., 1977. Theory and Applicability of a Recrystallized Grain Size Paleopiezometer, in: Wyss, M. (Ed.), *Stress in the Earth*. Birkhäuser Basel, pp. 227-244.
- Urai, J., Means, W., Lister, G., 1986. Dynamic recrystallization of minerals. *Mineral and Rock Deformation: Laboratory Studies: The Paterson Volume*, 161-199.
- van der Molen, I., 1985. Interlayer material transport during layer-normal shortening. Part II. Boudinage, pinch-and-swell and migmatite at Søndre Strømfjord Airport, West Greenland. *Tectonophysics* 115, 297-313.
- van Gool, J.A.M., Marker, M., 2007. Explanatory notes to the Geological map of Greenland, 1:100 000, Ussuit 67 V.2 Nord, in: Garde, A.A. (Ed.), *Geological survey of Denmark and Greenland Map Series 3*. Geological Survey of Denmark and Greenland (GEUS), Denmark.
- van Roermund, H., 2009. Mantle-wedge garnet peridotites from the northernmost ultra-high pressure domain of the Western Gneiss Region, SW Norway. *European Journal of Mineralogy* 21, 1085-1096.
- Vergnolle, M., Pollitz, F., Calais, E., 2003. Constraints on the viscosity of the continental crust and mantle from GPS measurements and postseismic deformation models in western Mongolia. *Journal of Geophysical Research: Solid Earth* 108, n/a-n/a.
- Voigt, W., 1928 *Lehrbuch der Kristallphysik*. Teubner, Leipzig, Germany.
- Warren, J.M., Hirth, G., 2006. Grain size sensitive deformation mechanisms in naturally deformed peridotites. *Earth and Planetary Science Letters* 248, 438-450.

- Watts, M.J., Williams, G.D., 1983. Strain geometry, microstructure and mineral chemistry in metagabbro shear zones: a study of softening mechanisms during progressive mylonitization. *Journal of Structural Geology* 5, 507-517.
- Weinberg, R.F., Regenauer-Lieb, K., Rosenbaum, G., 2007. Mantle detachment faults and the breakup of cold continental lithosphere. *Geology* 35, 1035-1038.
- Wheeler, J., Prior, D., Jiang, Z., Spiess, R., Trimby, P., 2001. The petrological significance of misorientations between grains. *Contrib Mineral Petrol* 141, 109-124.
- Whitney, D.L., Evans, B.W., 2010. Abbreviations for names of rock-forming minerals. *American mineralogist* 95, 185.
- Wood, B.L., 1972. Metamorphosed ultramafites and associated formations near Milford Sound, New Zealand. *New Zealand Journal of Geology and Geophysics* 15, 88-128.
- Yamasaki, T., Houseman, G.A., 2012. The crustal viscosity gradient measured from post-seismic deformation: A case study of the 1997 Manyi (Tibet) earthquake. *Earth and Planetary Science Letters* 351–352, 105-114.
- Zhong, S.J., Yuen, D.A., Moresi, L.N., 2007. 7.05 - Numerical Methods for Mantle Convection A2 - Schubert, Gerald, *Treatise on Geophysics*. Elsevier, Amsterdam, pp. 227-252.
- Zuber, M.T., Parmentier, E.M., 1986. Lithospheric necking: a dynamic model for rift morphology. *Earth and Planetary Science Letters* 77, 373-383.
- Zulauf, J., Zulauf, G., 2005. Coeval folding and boudinage in four dimensions. *Journal of Structural Geology* 27, 1061-1068.

Figure Labels:

Figure 1. (a) Geological map of the Anita Shear Zone (Turnbull et al., 2010), with the Anita Ultramafics layer re-interpreted by the authors using satellite imagery, structural data from the authors, Czertowicz et al. (2016a) and Klepeis et al. (1999) and vegetation variations; structural data included on the map is from Klepeis et al. (1999), geological unit names follow the terminology of Bradshaw (1990), Thurso Gneiss and St Anne Gneiss (paragneiss), Jagged Gneiss (orthogneiss); B_1 indicates the boundaries used for tortuosity analysis (see text for details); inset shows the

location of ASZ within New Zealand; blue, red and yellow arrows indicate a neck, swell and a thick neck (see text for details), respectively; (b) example of outcrop scale pinch and swell structure from St Anne Point (SAP, see (a) just off map to N), displaying foliation parallel to the swell boundary (image from Gardner et al., 2015; their Fig.2); this feature is used to interpret orientation of unit boundaries on the large scale (e.g. B₁ in (a)); (c) sketch of (b), location of inferred localisation planes are indicated by dashed red lines.

Figure 2. Details of pinch and swell structure near Lake Ronald; for location see Fig. 1 stippled box. (a) Aerial photograph (Google Earth, 2016) with superimposed unit boundaries and structural data for lineations, foliations and compositional banding. All data are authors' measurements except one at SW of lake from Czertowicz et al. (2016c); (b) geological map depicting high strain zones (HSZ) (edges indicated by red dashed lines in the Anita Ultramafics and black dotted line in the Jagged Gneiss) with approximate measured widths; boundaries between Anita Ultramafics and adjacent gneisses used for tortuosity analysis (B₂, black dashed line; see text for details) using vegetation demarcation and structural measurements shown in (a). Sample locations are provided; note that for the low strain Jagged Gneiss sample (AS1315F) the location is inferred. Unit colours are the same as for Figure 1; star is viewpoint for (c); general direction of extension associated with pinch and swell structure formation is indicated by double sided arrow; (c) field photograph showing the field area looking to the SW showing the boundaries of Anita Ultramafics and adjacent gneisses (d) sketch of (c); note the steep boundary of the ultramafic unit.

Figure 3. Outcrop photos from across the ASZ, arranged NW to SE (see text for details); foliation shown by double parallel lines. (a) HSZ sample of Thurso Gneiss, is a fine grained, high strain paragneiss with dark to light bands up to 5 mm wide defining the foliation; (b) Anita Ultramafics; HSZ near the Thurso Gneiss, is a fine grained olivine with few elongated porphyroclasts up to 2 mm in size and layers of oxides (dark) ~1 mm wide defining the foliation; (c) Anita Ultramafics; low strained sample from the centre, has a large number of porphyroclasts of 5 - 7 mm size with a poorly defined foliation; (d) Anita Ultramafics; HSZ near the Jagged Gneiss, is a fine grained olivine with few elongated porphyroclasts up to 1.5 mm in size defining the foliation; (e) Jagged Gneiss, HSZ sample, is a fine grained orthogneiss with well-defined dark and light bands exhibiting 1 mm spacing, defining the high strain foliation.

Figure 4. Examples of compositional banding from the centre of the Anita Ultramafics; (a) 20 cm wide band of harzburgite within a harzburgite that exhibits more than 15% talc. Both types of harzburgite have large olivine porphyroclasts up to 8mm in size; talc has variable area % and forms thin disconnected bands which define the foliation; (b) harzburgite similar to the central band shown in (a); here it is characterized by the presence of bands up to 10cm in width of clinopyroxene-rich lherzolite. In this lherzolite, large grains of clinopyroxene are seen (up to 5mm), standing prominently where lichen preferentially grows (dark colour).

Figure 5. ASZ thin sections of representative rock types; scale is the same for all samples. << in red indicate presence of subgrain boundaries; << in yellow indicate

examples of lobate boundaries (see text for details); mineral abbreviations per Whitney and Evans (2010). (a) Thurso Gneiss (paragneiss; AS1304E); Bt is wrapping around Qz and Pl; (b) Anita Ultramafics (AS1305A2); HSZ near the Thurso Gneiss boundary; it is fine grained and exhibits a well-defined shape preferred orientation but a general lack of large relict porphyroclasts; (c) Anita Ultramafics (AS1309), centre of unit; photomicrograph shows a typical microstructure with a large, relict Ol grain in bottom right (> 5mm as measured on the thin section) surrounded by a tail of fine grained Ol which is imbedded in a finer grained matrix including both En and Ol; recrystallized Ol is outlined by dashed white lines, inset shows an example of a lobate boundary; note that the large relict Ol grain exhibits clear internal deformation including subgrain boundaries; (d) Anita Ultramafics (AS1330); HSZ near the Jagged Gneiss boundary; it is fine grained with elongate larger, remnant olivine grains; (e) Jagged Gneiss (orthogneiss; AS1316B) from HSZ adjacent to Anita Ultramafics, inset shows example of a lobate boundary; (f) Jagged Gneiss (AS1315F; low strain sample; it is coarser grained than its HSZ equivalent, exhibiting abundant undulose extinction, subgrains and irregular boundaries.

Figure 6. EBSD data for ASZ high strain zone (HSZ) gneiss samples; (left) phase map with grain, subgrain and Dauphiné twin boundaries shown; note that the shown maps are a subset of the complete EBSD map acquired; note orientation of sample reference frame with X parallel to lineation and XY parallel to the foliation plane; pole figures are equal area, lower hemisphere representations using one point per grain for the whole acquired map; average recrystallised grain sizes for specified mineral fraction with number used for the calculation are provided in italics, error margins are 1 sd; (right) misorientation angle distributions (MAD) histograms showing adjacent

(or correlated) grain pairs in blue and random (or uncorrelated) grain pairs in red with the theoretical random distribution displayed as a black line. M-index values (M_i) are listed on the histograms (see text for details). (a) Thurso Gneiss; (b) Jagged Gneiss; note on EBSD map, the largest quartz grain at top right has an overlay of relative crystal orientation change with respect to the orientation marked with the white cross (0° black), up to 20° variation (aqua) showing significant internal deformation; in quartz pole figure data from the same large Qz grain is overlain on the bulk pole figure.

Figure 7. EBSD data of the variably deformed Anita Ultramafics; (left) phase map with grain and subgrain boundaries shown; note that the shown maps are a subset of the complete EBSD map acquired; representative large, porphyroclastic olivine grains have an overlay of relative crystal orientation change with respect to the orientation marked with a white cross (0° black), up to 10° variation (aqua) in (b) and up to 20° variation in (c) and (d); note orientation of sample reference frame with X parallel to lineation and XY parallel to the foliation plane; pole figures are equal area, lower hemisphere representations using one point per grain for the whole acquired map and are overlaid by the large olivine grains depicted in the phase maps (aqua); average recrystallised grain sizes for specified mineral fraction with number used for the calculation are provided in italics, error margins are 1 sd; percentage of large, relict olivine grains ($> 100 \times 100 \mu\text{m}^2$) is included; (right) misorientation angle distributions (MAD) histograms showing adjacent (or correlated) grain pairs in blue and random (or uncorrelated) grain pairs in red with the theoretical random distribution displayed as a black line; Shape preferred orientation (SPO) data is half rose diagrams showing angles of grain orientation where 90° is parallel to lineation;

M-index values (M_i) are listed under the SPO diagrams (see text for details). (a) and (b) are samples near the Thurso Gneiss boundary where (a) is closest to the Thurso gneiss boundary; (c) sample from the centre and (d) sample next to the Jagged Gneiss boundary.

Figure 8. Summary of Anita Ultramafics results and interpretation of deformation mechanisms arranged as a cross-section across the Anita Ultramafics from SE-NW. (a) Graph of M-Index for olivine and enstatite in each sample from across the Anita Ultramafics; (b) mineral recrystallised grain sizes with 1sd error bars; (c) percentage remaining relict olivine grains; (d) olivine CPO type (Tommasi et al., 2000; Karato et al., 2008; Mainprice, 2015); (e) deformation mechanisms, xx denotes dislocation creep, // denotes grain boundary sliding (GBS) and mx is phase mixing, subscripts are mineral abbreviations; (f) Inferred stress exponent (n) used as input into the numerical modelling.

Figure 9. Numerical setup and general results. (a) Initial Underworld numerical model setup showing equivalent rock units, stress exponent (n) and viscosity coefficient ratios for Layer B to Layer A and C (R_{VA} and R_{VC} , respectively); (b) results from kilometre-scale Underworld numerical model of the developing pinch and swell structures at stretch 1.6, 2.3 and 3.2 for the model where $R_{VA} = 5$ and $R_{VC} = 80$ (marked by star on Fig. 10a). Dashed box indicates area displayed in stretch 3.2 plots, stretching direction is indicated by double ended arrow, blue, red and yellow arrows indicate examples of a neck, swell and thick neck (see text for details), respectively; (c) differential stress across the numerical model at stretch 1.05; (d)

differential stress across the swell structure marked by red line in stretch 2.3, increased stress (arrows) occurs either side of the central unit swell boundaries at stretch 2.3.

Figure 10. Numerical model results; (a) tortuosity difference, which is a measure of shape asymmetry (see text for details) for the models; R_{VA} is the ratio of Layer B to Layer A (the weakest layer) viscosity coefficient; R_{VC} is the ratio of Layer B to Layer C viscosity coefficient (see inset), also see text for further details; field derived tortuosity difference for the ASZ (T_{D1} and T_{D2}) are plotted for comparison; symbols and pinch and swell structures correspond to different R_{VA} and R_{VC} as provided in (b); star marks R_{VA} of 80 and R_{VC} of 5 which results in a tortuosity difference similar to that of the ASZ; (b) examples of the pinch and swell structures formed at stretch 2.3 for comparison, corresponding resultant tortuosity difference for the different R_{VA} and R_{VC} values are marked on (a).

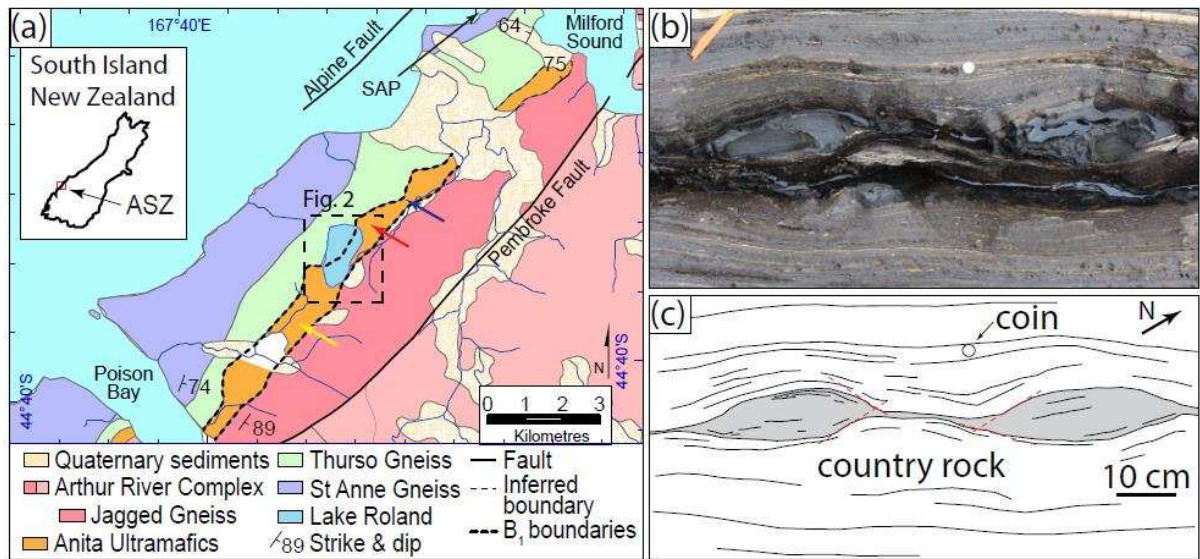


Fig. 1

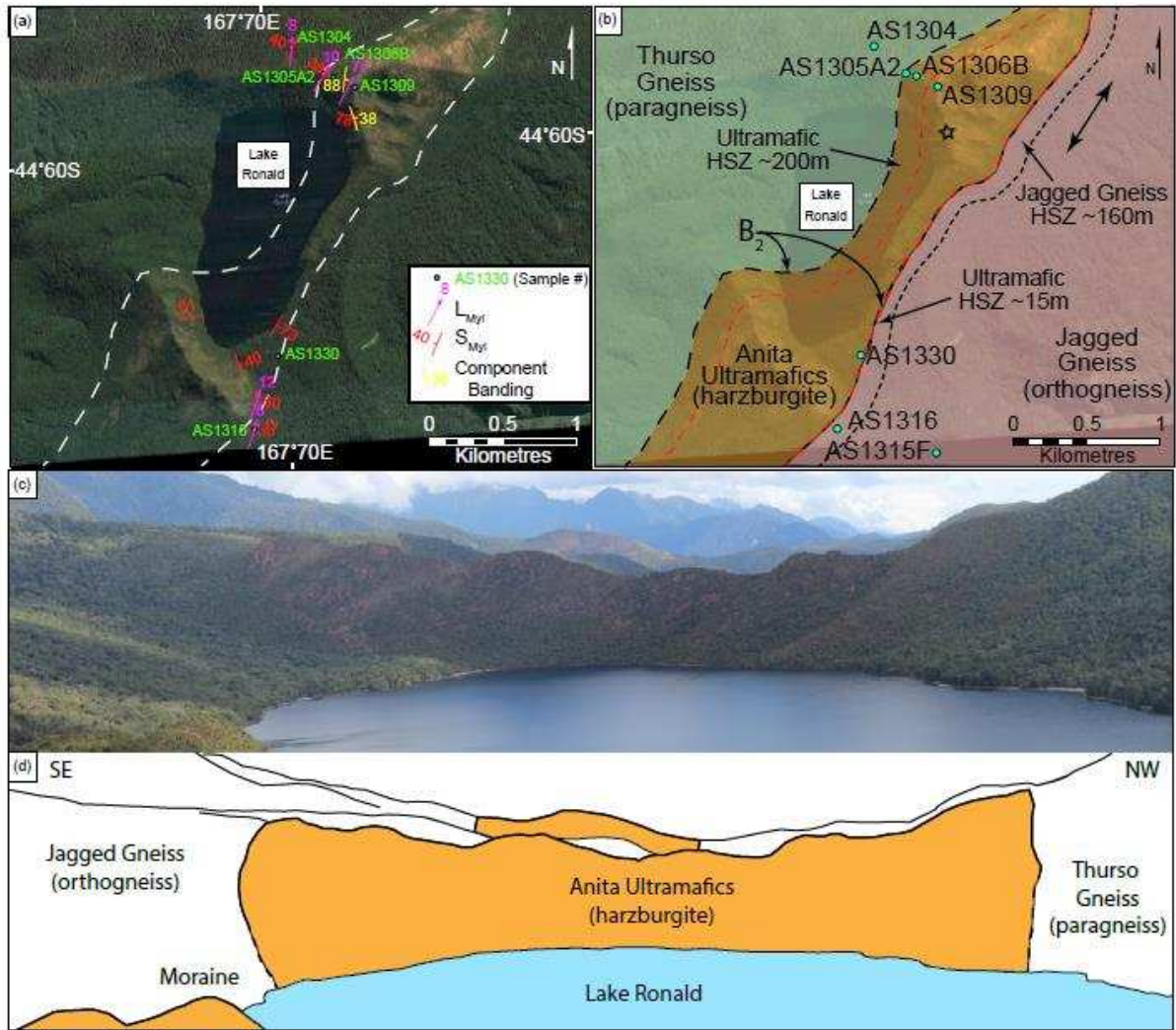


Fig. 2

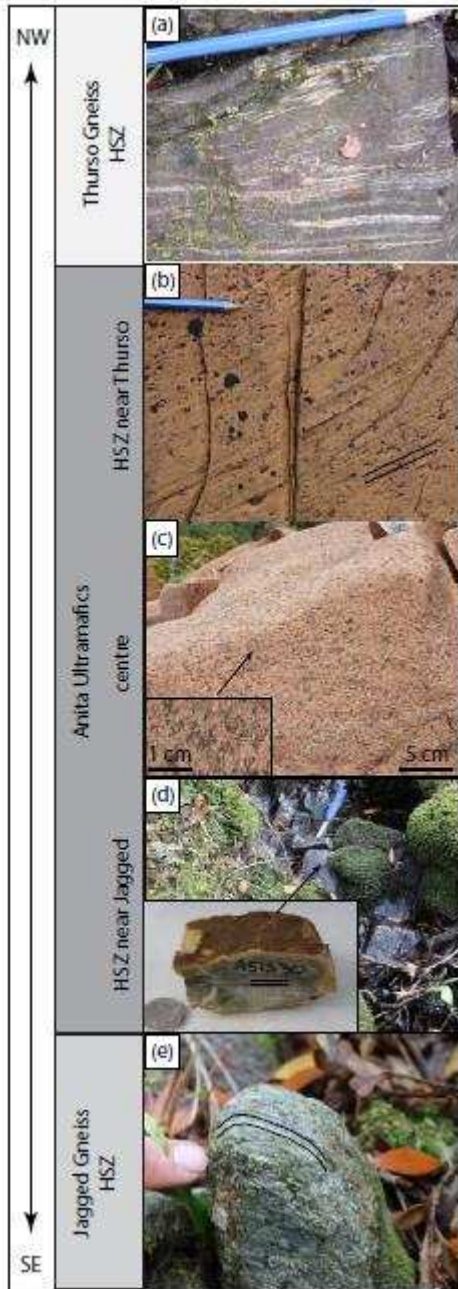


Fig. 3

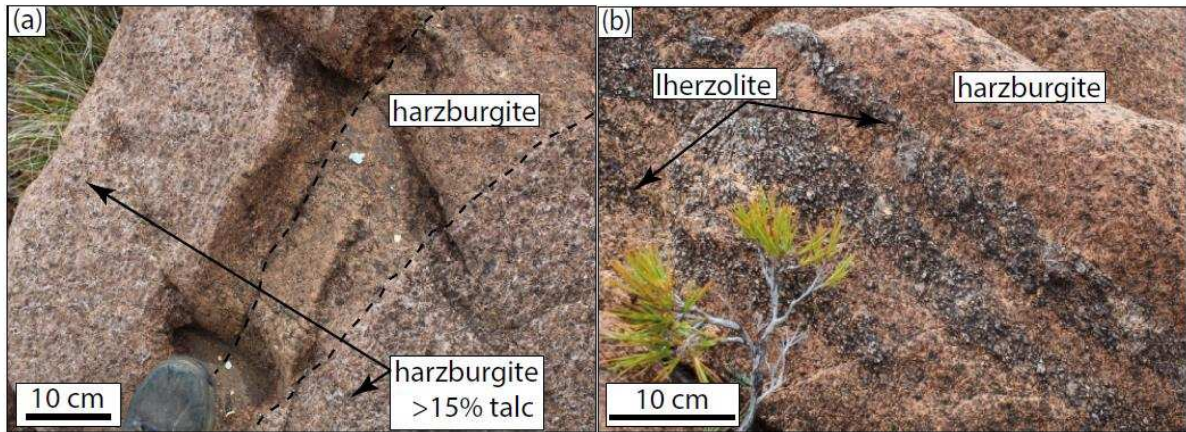


Fig. 4

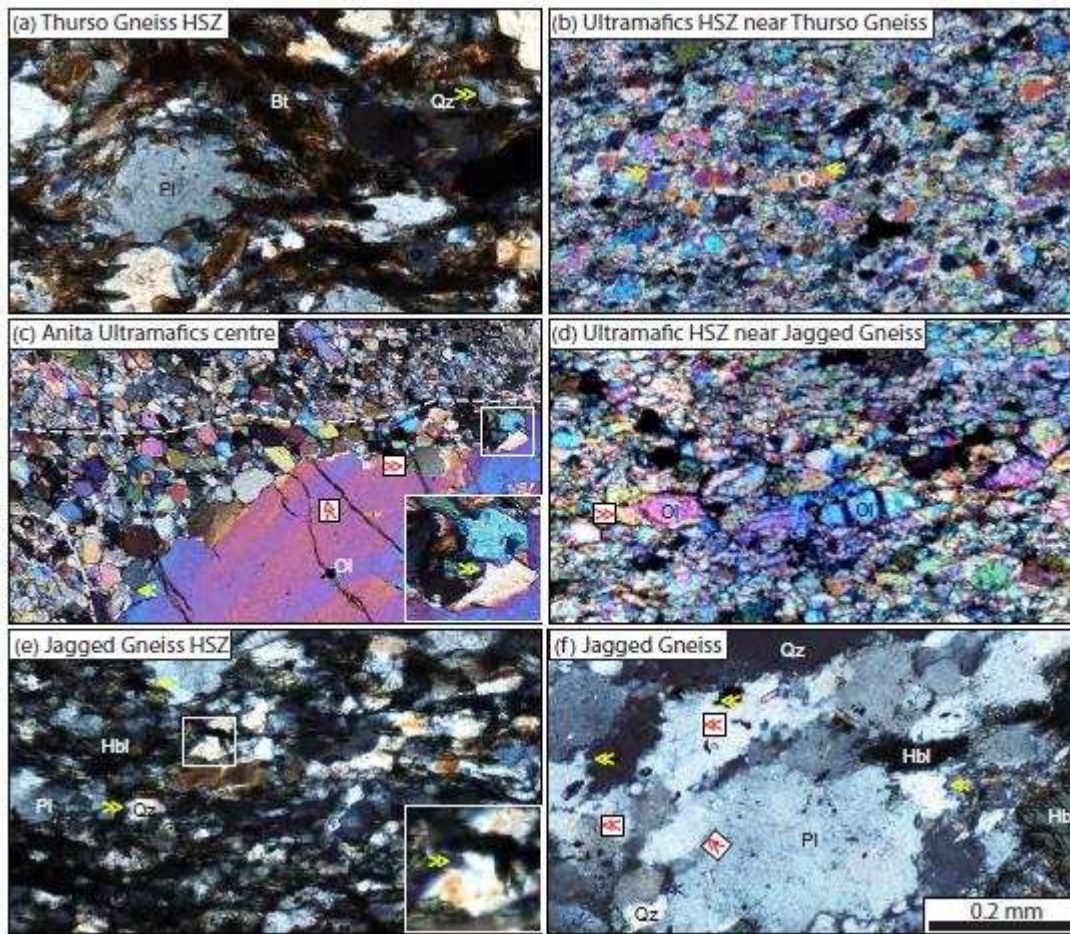


Fig. 5

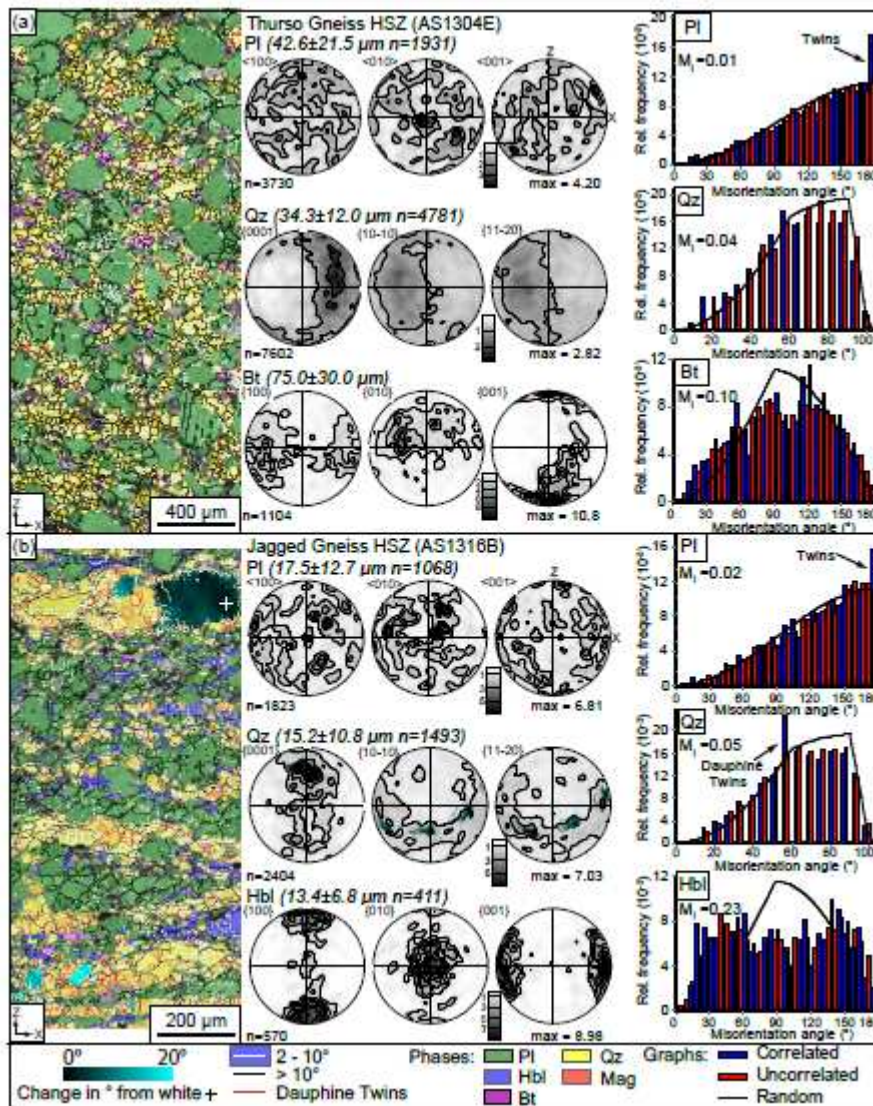


Fig. 6

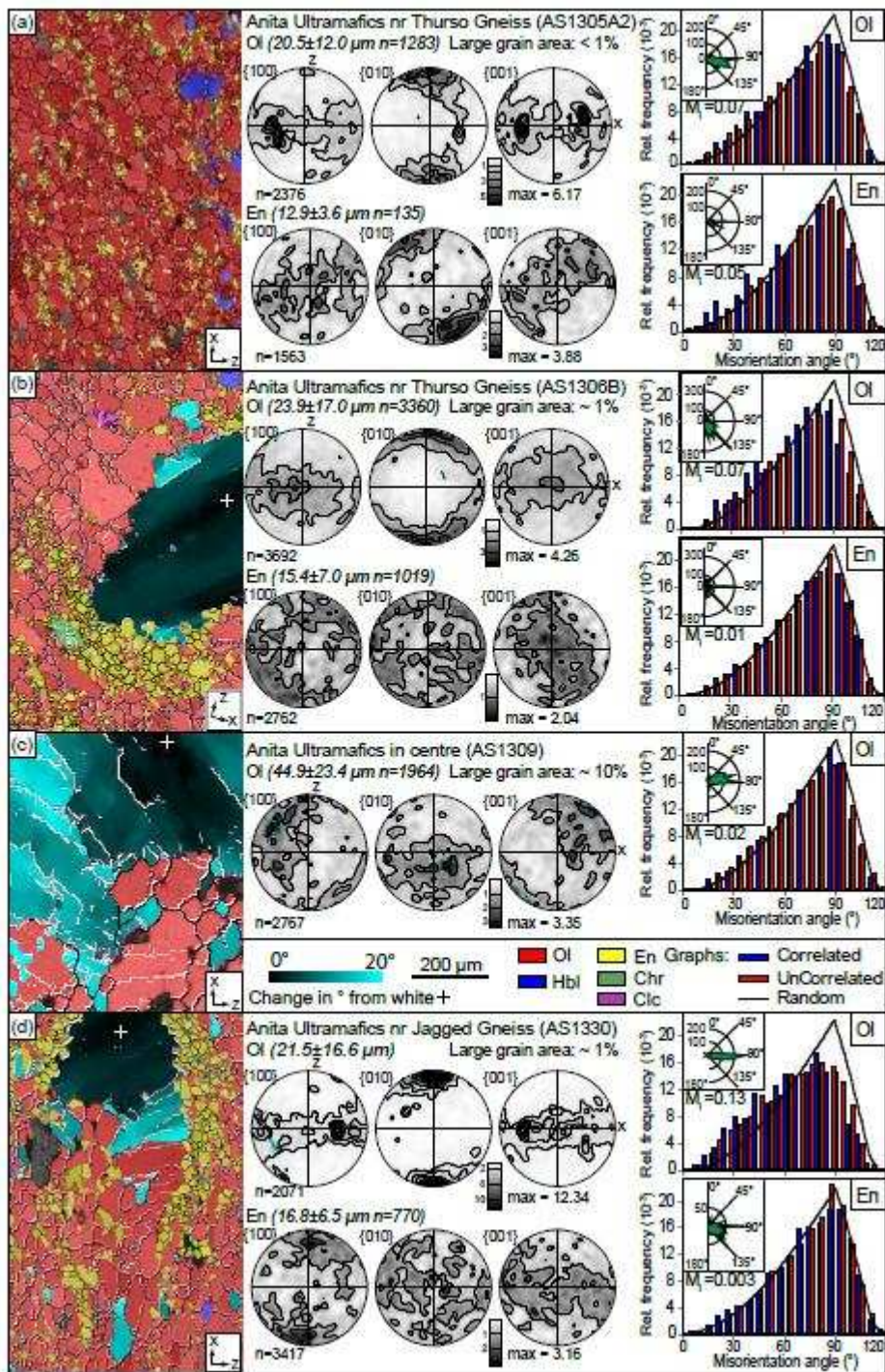


Fig. 7

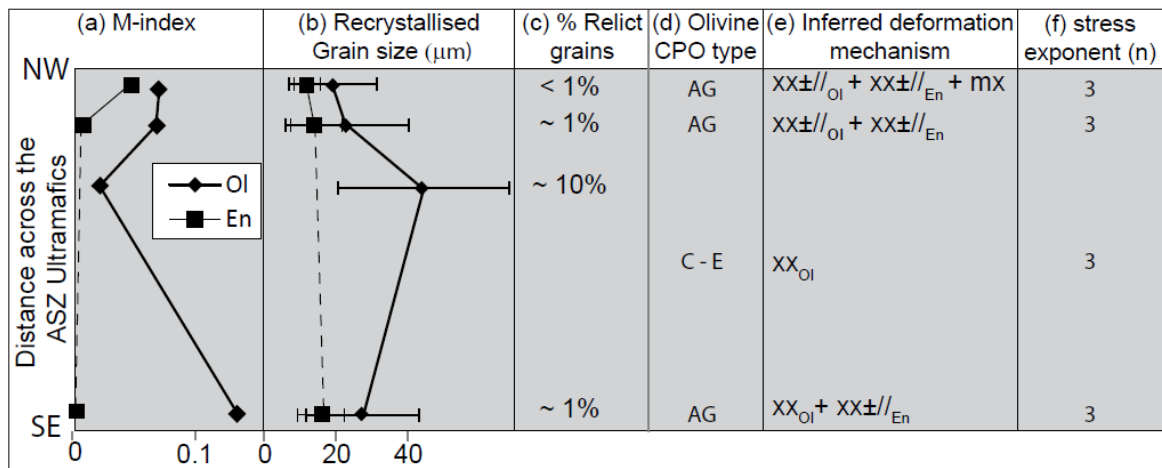


Fig. 8

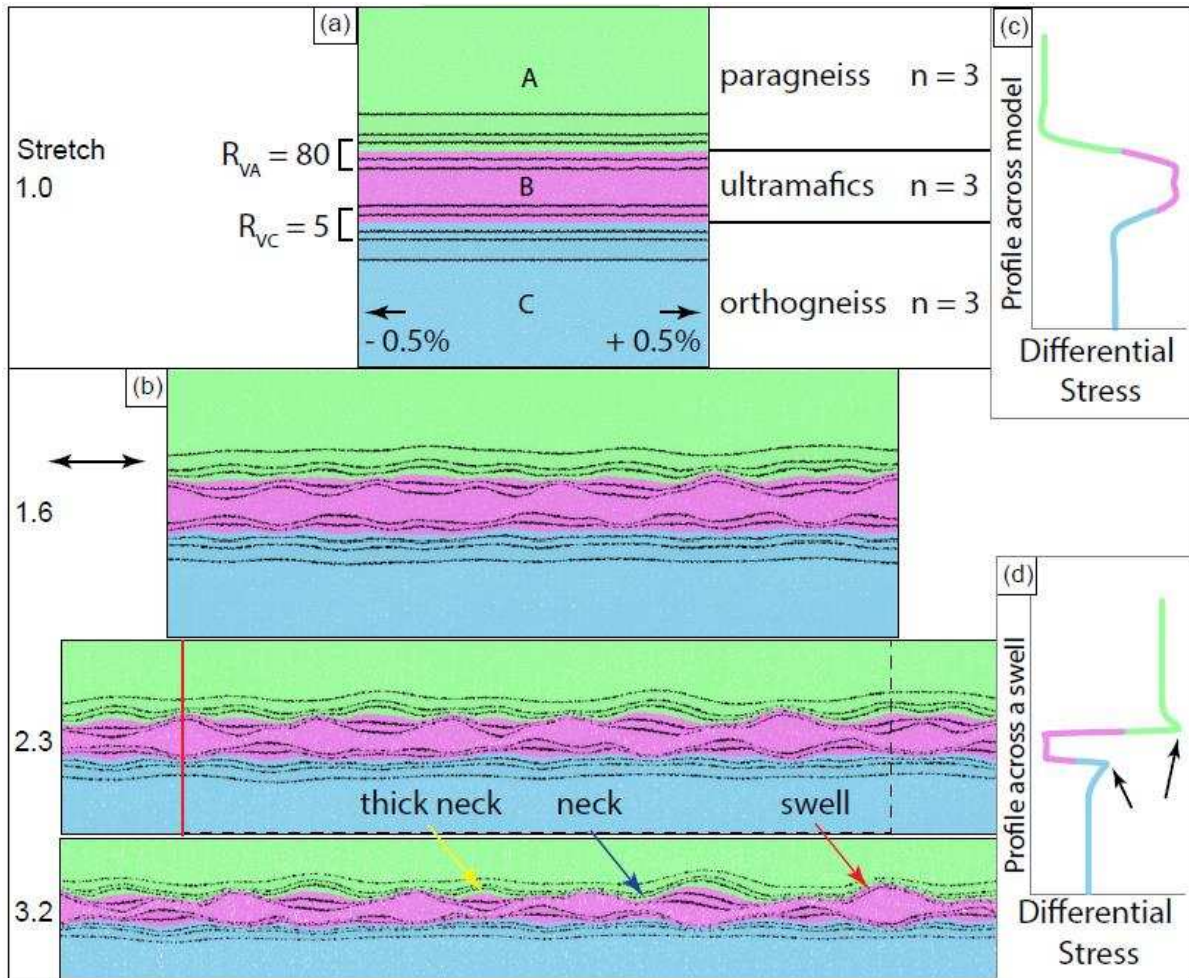


Fig. 9

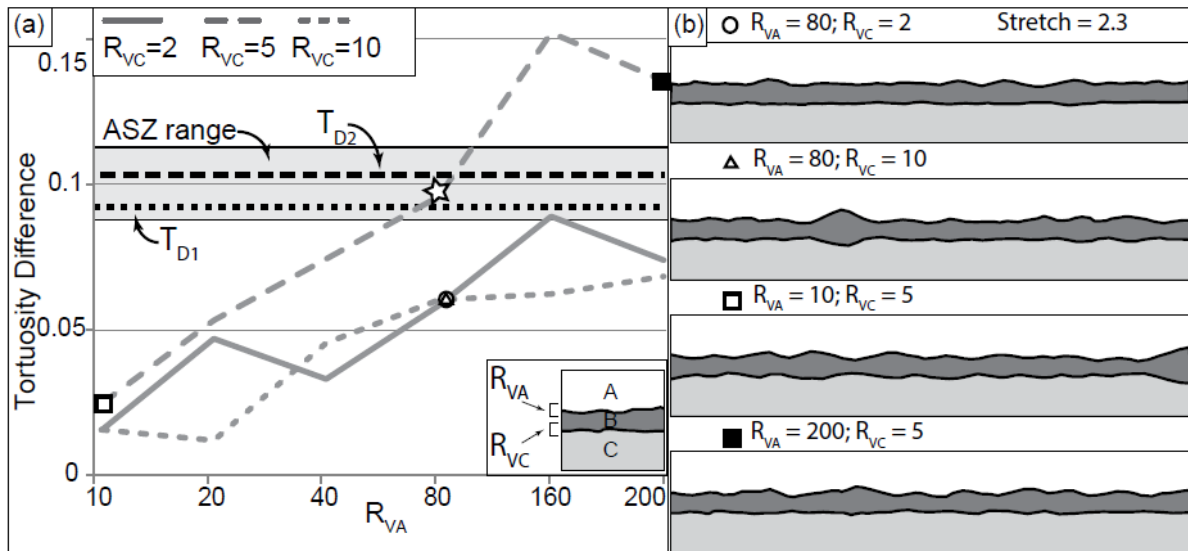


Fig. 10

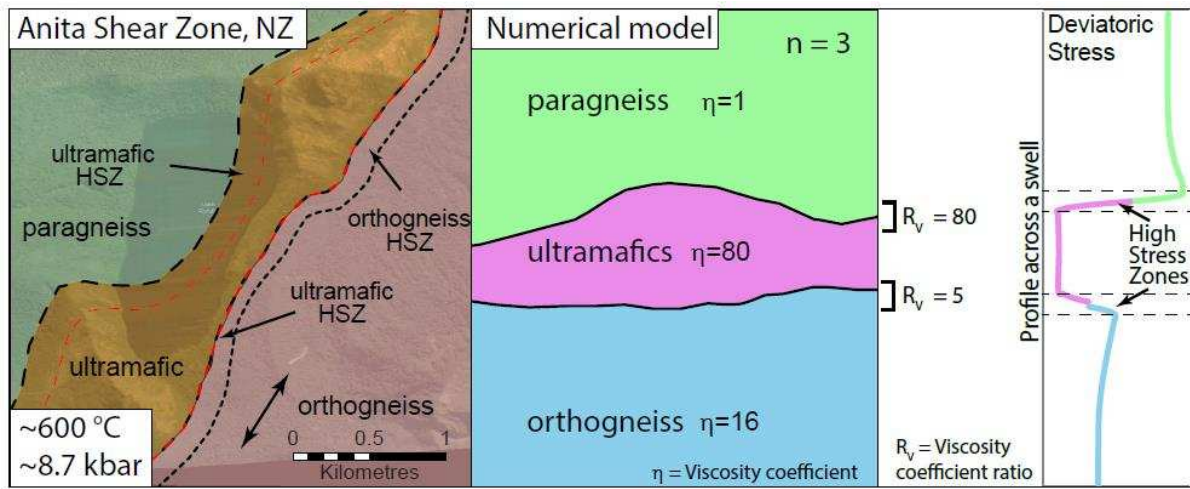
| Unit | Sample # | Main minerals | Mode | Recrystallised Grain size (μm) | Number of grains | Grain Aspect Ratio | M-Index | Intracrystalline deformation |
|-------------------|------------------------------------|---------------|------|---|------------------|--------------------|---------------|--|
| Thurso Gneiss | AS1304 | Pl | 41% | 42.6 ± 21.5 | 1931 | 1.6 ± 0.5 | 0.01 | undulose extinction, subgrains & deformation twins |
| | | Qz | 31% | 34.3 ± 12.0 | 4781 | 1.6 ± 0.5 | 0.04 | undulose extinction, subgrains & Dauphiné twins |
| | | Bt | 22% | 75 ± 30 | | 1.6 ± 0.6 | 0.10 | |
| | | Other | 6% | | | | | |
| Anita Ultramafics | AS1305A2 | Ol | 85% | 20.0 ± 12.0 | 1283 | 1.8 ± 0.5 | 0.07 | rare porphyrocasts: undulose extinction & subgrains; fine bands of opaques |
| | | En | 11% | 12.9 ± 3.6 | 135 | 1.7 | 0.05 | dispersed in Ol |
| | | Other | 4% | | | | | |
| | AS1306B | Ol | 81% | 23.9 ± 17.0 | 3360 | 1.7 ± 0.3 | 0.07 | porphyrocasts: undulose extinction & subgrains; fine bands of opaques |
| | | En | 15% | 15.4 ± 7.0 | 1019 | 1.6 | 0.01 | forms bands in Ol |
| | | Other | 4% | | | | | |
| | AS1309 | Ol | 85% | 44.9 ± 23.4 | 1964 | 1.7 to 2.2 | 0.02 | porphyrocasts: undulose extinction & subgrains |
| | | Other | 15% | | | | | |
| | AS1330 | Ol | 80% | 28.2 ± 15.5 | 1370 | 2.2 ± 1.0 | 0.13 | porphyrocasts: undulose extinction & subgrains |
| | | En | 13% | 16.8 ± 6.5 | 770 | 1.6 ± 0.5 | 0.003 | forms bands in Ol |
| | | Other | 7% | | | | | |
| | Jagged Gneiss (high strain sample) | AS1316B | Pl | 35% | 17.5 ± 12.7 | 1068 | 1.7 ± 0.6 | 0.02 |
| Qz | | | 39% | 15.2 ± 10.8 | 1493 | 1.8 ± 0.6 | 0.05 | minor undulose extinction, subgrains & Dauphiné twins |
| Hbl | | | 10% | 13.4 ± 6.8 | 411 | 2.2 ± 1.1 | 0.23 | subgrains |
| Other | | | 16% | | | | | |

Table 1. Summary of microstructural data

| Variable | Olivine | Anorthite |
|---|---------|-----------|
| Material constant ($\text{Mpa}^{-n-r} \mu\text{m}^p/\text{s}$) ¹ | 90 | 398 |
| Stress exponent ¹ | 3.5 | 3 |
| Water fugacity exponent ¹ | 1.2 | |
| Activation energy (kJ/mol) ¹ | 480 | |
| Activation volume (cm^3/mol) ¹ | 11 | |
| Pressure (GPa) ^{2,3,4} | 0.87 | |
| Temperature (°K) ^{2,3,4} | 873 | |
| Water fugacity (MPa) ⁵ | 1000 | |
| Activation enthalpy (kJ/mol) ⁶ | | 356 |

Table 2. Values used in the calculation of viscosity of olivine-dominated Ultramafic unit and anorthite. References are: 1. Hirth and Kohlstedt (2003) 2. (Clarke et al., 2000); 3. Czertowicz et al. (2016); 4. Klepeis et al. (1999); 5. water fugacity is based on water activity of 0.3 as the Ultramafic unit contains pre-D₃ component banding with variable amounts of talc, a hydrous phase; 6. Rybacki and Dresen (2004)

Graphical abstract



Highlights

Pinch and swell shape asymmetry - a gauge for relative bulk viscosity

Kilometre scale structure allows viscosity determination of polymineralic rocks

Mid-crustal orthogneiss is up to 3 times more competent than paragneiss

In rock packages differential stress increases towards lithological boundaries

ACCEPTED MANUSCRIPT